Engineering Structures 360 (2026) 122811

Contents lists available at ScienceDirect

Engineering Structures

journal homepage: www.elsevier.com/locate/engstruct

Testing and analysis of additively manufactured aluminium I- and C-section stub columns

Wenxuan Hong [a,*], Eman Mansour [b], Marina Bock [c], Leroy Gardner [a]

[a] Department of Civil and Environmental Engineering, Imperial College London, London, SW7 2AZ, United Kingdom
[b] School of Architecture and Built Environment, University of Wolverhampton, Wolverhampton, WV10 0JP, United Kingdom
[c] Department of Civil Engineering, Aston University, Birmingham, B4 7ET, United Kingdom

ARTICLE INFO

Keywords:
Additive manufacturing
Aluminium
C-section
Design methods
I-section
Powder bed fusion
Stub column tests
Tensile coupon tests

ABSTRACT

Laser beam powder bed fusion (PBF-LB/M) has become more prevalent in recent years, favoured for its ability to produce intricate geometries with high dimensional accuracy. Aluminium alloys are widely applied in the aerospace, automotive and construction industries owing to their high strength-to-weight ratios, good durability, corrosion resistance and ease of fabrication. To date, there is, however, a dearth of experimental data relating to the structural performance of PBF-LB/M aluminium elements, which is preventing the wider adoption of this technology in construction applications. To address this gap, an experimental investigation into the mechanical properties and structural performance of the PBF-LB/M AlSi10Mg I- and C-section stub columns has been conducted and is presented in this paper. Seven I-section and seven C-section stub columns were tested under axial compression. The geometric dimensions and the local imperfections of the test specimens were measured using 3D laser scanning. Digital image correlation (DIC) was employed to capture the surface deformation field during testing. In the present paper, following a description of the specimen manufacture, the experimental programme is described, the test results are analysed and the applicability of EN 1999-1-1:2023 (EC9), the Aluminum Design Manual 2020 (ADM), the Direct Strength Method (DSM) and the Continuous Strength Method (CSM) to the design of PBF-LB/M aluminium I- and C-sections is assessed by comparing the test results with the associated design predictions. The performances of the PBF-LB/M aluminium I- and C-sections were found generally to align with the trend of the conventionally-manufactured aluminium I- and C-sections. All of the four design approaches yield safe-sided resistance predictions, among which the CSM provides the most accurate predictions by accounting for the effects of strain hardening in the PBF-LB/M aluminium. The experimental results provide valuable benchmark data for additively manufactured aluminium structural cross-sections and demonstrate that the existing aluminium design methods can be safely extended to predict the cross-sectional resistance of PBF-LB/M AlSi10Mg I- and C-sections in compression.

1. Introduction

Additive manufacturing (AM) has developed rapidly over the past decade and is now recognised as a promising route for the production of high-performance engineering components. Unlike conventional manufacturing methods, AM enables the fabrication of intricate geometries with minimal material wastage and without the constraints of traditional forming or extrusion processes. These attributes are particularly attractive in sectors such as aerospace, where weight saving is of paramount importance, and in structural engineering, where geometric efficiency and bespoke design solutions can lead to improved structural performance and lighter structures with lower embodied carbon [1–3]. Among the available metal AM technologies, laser beam powder bed fusion (PBF-LB/M [4]) has emerged as one of the most advanced and widely used, offering high dimensional accuracy, good repeatability and suitability for structural alloys. At present, the limited build envelope and higher production cost compared with conventional extrusion make the use of PBF-LB/M for full-length structural members economically challenging. In practice, its application is more likely to be in intricate nodes and optimised components, where the geometric freedom and dimensional accuracy offered by PBF-LB/M can justify the higher manufacturing cost [1,5].

Aluminium alloys have been of longstanding interest to both the aerospace and structural engineering sectors owing to their excellent strength-to-weight ratios, corrosion resistance and favourable fabrication characteristics [6–8]. Research on PBF-LB/M aluminium alloys, such as AlSi10Mg, has shown that they can achieve comparable or superior hardness and strength compared to conventionally-manufactured

* Corresponding author.
E-mail address: wenxuan.hong21@imperial.ac.uk (W. Hong).

https://doi.org/10.1016/j.engstruct.2026.122811
Received 20 January 2026; Received in revised form 19 March 2026; Accepted 20 April 2026
Available online 23 April 2026

Table 1
Chemical composition (in % by weight) of the AlSi10Mg powder, as reported by the manufacturer.

Si	Fe	Cu	Mn	Mg	Ni	Zn	Pb	Sn	Ti	Al
9.0–11.0	0.55	0.05	0.45	0.25–0.45	0.05	0.10	0.05	0.05	0.15	Balance

counterparts, provided that optimal process parameters are used [9–12]. Moreover, studies have extensively investigated the anisotropic behaviour of AM aluminium alloys, linking their directional properties to process parameters such as scan strategy [13,14]. However, the majority of these studies have focused on material characterisation at a coupon level, while investigations at a structural level remain scarce.

Although additive manufacturing enables the fabrication of geometrically complex and structurally optimised components [1,15], it is essential to first examine the structural behaviour of additively manufactured members with conventional cross-section configurations. Such sections may themselves be employed in optimised structural systems and also provide a means of isolating the influence of the manufacturing route on the structural behaviour. Existing structural level studies on PBF-LB/M aluminium members have primarily focused on tubular sections, such as the experimental work by Bock et al. [16] on AM circular hollow sections and Zhang et al. [17], Mansour et al. [18] on AM square hollow sections. Compared with tubular sections, open thin-walled sections such as I- and C-profiles exhibit different structural behaviour and are generally more susceptible to local buckling, with interaction between individual plate elements [19]. Despite their potential widespread use as structural members and stiffeners in lightweight aluminium structures in aerospace and structural engineering applications, the structural behaviour of PBF-LB/M aluminium open sections has received limited attention. For this reason, I- and C-section configurations were selected in the present study as representative open sections, whose well-understood structural behaviour enables direct comparison with conventionally manufactured aluminium members.

In the present study, an experimental investigation was conducted on PBF-LB/M AlSi10Mg I- and C-section stub columns to examine their local buckling responses and the associated design resistance predictions, thereby providing new structural level test data for additively manufactured aluminium members. The experimental programme included tensile coupon tests to determine the mechanical properties, 3D laser scanning to measure the initial geometric imperfections and stub column tests to investigate the local buckling behaviour and load-carrying capacity of the PBF-LB/M AlSi10Mg I- and C-sections. Digital image correlation (DIC) was employed to monitor the surface deformations of the tensile coupons and the stub columns during testing. The test results were analysed and compared (alongside existing experimental data) with the design resistance predictions obtained using EN 1999-1-1:2023 (EC9) [20], the Aluminum Design Manual 2020 (ADM) [21], the Direct Strength Method (DSM) [21] and the Continuous Strength Method (CSM) [22].

2. Specimen manufacture and preparation

Six tensile coupons, seven I-sections and seven C-sections were manufactured using an EOS M 290 machine [23], featuring a 250 mm × 250 mm × 200 mm building space and a 400 W Yb-fibre laser beam, in the metal printing laboratories at the School of Engineering of the University of Wolverhampton. AlSi10Mg powder was employed as the feedstock material, which is commonly used in aluminium additive manufacturing, offering superior mechanical properties over the conventionally-manufactured (i.e. cast and powder metallurgy) counterparts [24–27]; the chemical composition of the AlSi10Mg powder is detailed in Table 1.

Two 250 mm × 250 mm aluminium plates were used as the building platform for the coupons and the stub columns. Initially, a layer of AlSi10Mg powder was evenly spread onto the building platform by the recoating blades. The high-energy Gaussian laser beam selectively melted and fused the powder particles onto the building plate, along the scanning path derived from the sliced cross-sections of the 3D digital models, as shown in Fig. 1(a). Subsequently, the building platform was lowered by a layer thickness of 30 μm, and the recoating and scanning cycle was repeated until the completion of the target parts – see Fig. 1(b). The process parameters were set according to the manufacturer's specifications to ensure a final product density of 99.8%, as listed in Table 2. A bidirectional stripe scanning strategy was adopted, with a scanning rotation angle of 67° between layers to reduce residual stresses and thermal distortions.

Table 2
PBF-LB/M process parameters adopted in this study.

Process parameter	Details
Feedstock powder	AlSi10Mg
Laser power (W)	370
Laser spot diameter (μm)	100
Scanning speed (mm/s)	1300
Scanning rotation (°)	67
Hatch distance (μm)	190
Layer thickness (μm)	30
Preheated powder bed (°C)	35
Shielding gas mixture	>99.9%Ar

In order to investigate the potential anisotropic behaviour of the PBF-LB/M aluminium, tensile coupons of two nominal thicknesses (i.e. 3 mm and 6 mm) were built at orientations of $\theta = 0°$, 45° and 90°, as shown in Fig. 2(a), where θ is the angle between the longitudinal axis of the coupon and the scanning direction. Supporting structures were printed for the 45° and 90° coupons to stabilise the cantilevered sections, which were removed upon completion. The nominal dimensions of the tensile coupons are illustrated in Fig. 2(b). The stub column specimens were evenly spaced within the printing space, and were built perpendicularly to the building plate. The notations employed to describe the I- and C-section stub columns are shown in Figs. 3(a) and 3(b), respectively. Each tensile coupon specimen was labelled with an identifier (ID), e.g. 'T-3-90', where 'T' denotes tensile testing, '3' denotes a nominal thickness of 3 mm and '90' represents the $\theta = 90°$ orientation. The labelling system for the stub column specimens starts with the cross-section shape (i.e. 'I' and 'C' denote the I- and C-section, respectively), followed by a number to indicate the nominal cross-section size. The specimen ID and the nominal cross-section dimensions of the stub column specimens are listed in Table 3, where H_{nom} is the nominal height of the cross-section, b_{nom} is the nominal breadth, $t_{w,nom}$ is the nominal web thickness, $t_{f,nom}$ is the nominal flange thickness and L_{nom} is the nominal length. To relieve the residual stresses induced by the PBF-LB/M process, all the coupon and column specimens underwent a heat treatment at 300 °C for 2 h in air atmosphere with the building plates attached. The cooling scheme of the heat treatment was carried out by switching off the furnace after the specimens had been held at 300 °C for 2 h. The specimens were then allowed to cool naturally to room temperature inside the furnace chamber. Once room temperature was reached, the furnace chamber was opened and all specimens were removed. Subsequently, the coupons and the stub columns were detached from the building plates via electrical discharge machining. The overall length of the stub columns was set at 150 mm to include a representative local geometric imperfection pattern, while being short enough to prevent global buckling failure [28]. The ends of the column specimens were lapped flat and square to achieve a uniform compressive stress distribution during compressive testing. To achieve

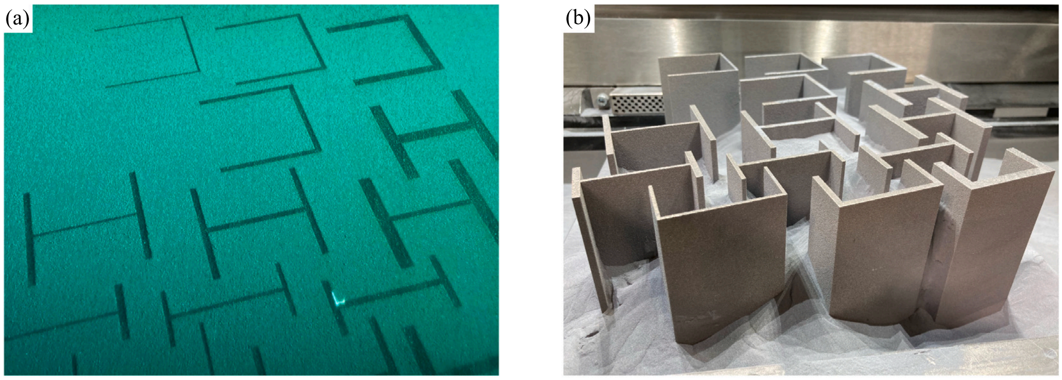

Fig. 1. I- and C-section stub columns: (a) during printing; (b) as manufactured on the building plate.

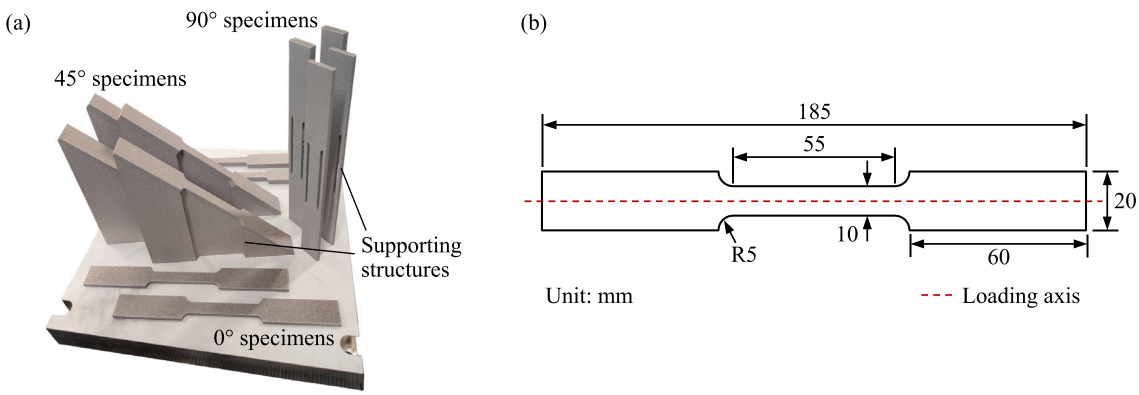

Fig. 2. Tensile coupons: (a) as manufactured on the building plate; (b) nominal dimensions.

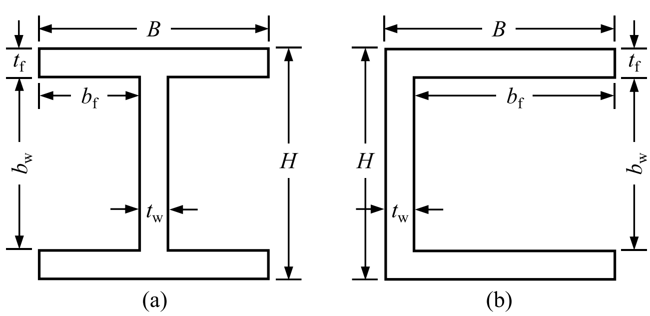

Fig. 3. Cross-section notations for (a) I-sections and (b) C-sections.

Table 3
Nominal cross-section dimensions of the I- and C-section stub columns.

Specimen ID	H_{nom} (mm)	b_{nom} (mm)	$t_{w,nom}$ (mm)	$t_{f,nom}$ (mm)	L_{nom} (mm)
I-1	25	50	3.0	3.0	150
I-2	25	50	1.5	1.5	150
I-3	25	50	2.0	2.0	150
I-4	50	50	6.0	6.0	150
I-5	50	50	6.0	3.0	150
I-6	50	50	3.0	3.0	150
I-7	50	50	3.0	1.5	150
C-1	25	50	5.0	5.0	150
C-2	25	50	3.0	3.0	150
C-3	25	50	1.5	1.5	150
C-4	50	50	5.0	5.0	150
C-5	50	50	3.0	3.0	150
C-6	50	50	2.5	2.5	150
C-7	50	50	1.5	1.5	150

the desired fixed boundary conditions and also prevent premature local failures at the specimen ends, a pair of stiffening plates with a thickness of 10 mm was affixed to the ends of C-sections using Araldite 2011 epoxy adhesive [29], as shown in Fig. 4; the end clamping approach has been successfully employed by Hong et al. [30].

3. Geometric analysis

3.1. Geometric properties

The geometric properties of the tensile coupons (i.e. the width and thickness within the parallel length) were measured prior to testing using a micrometre with a pair of point tips which was employed to eliminate measurement errors induced by the flared edges. Measurements of the width and the thickness were taken at five equally spaced locations along the parallel length to obtain the average cross-sectional area. The measured geometric properties of the tensile coupons within the parallel length are listed in Table 4, in which W_T is the average width, t_T is the average thickness and A_T is the average cross-sectional area.

For the stub columns, the geometric properties were determined using digital callipers, Archimedes' method and 3D laser scanning. The cross-section height H and breadth B as well as the overall length L of the stub column specimens were measured using a digital calliper. The mass of the column specimens M was measured with a digital scale, while the volume of the specimens was calculated by: $V = M/\rho$, where ρ is the average material density measured following the same approach as outlined in [31]. An average density ρ of 2.652 g/cm^3 was obtained, which is comparable to the solid AlSi10Mg density of 2.67

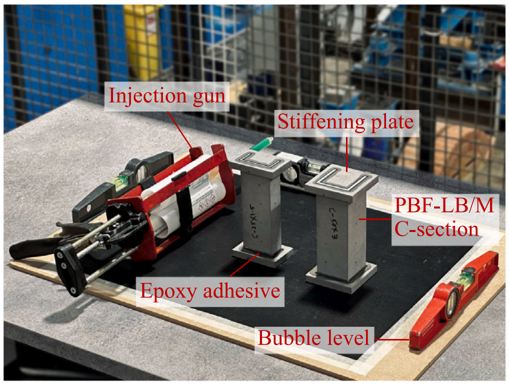

Fig. 4. Reinforcing of ends of PBF-LB/M C-section stub columns.

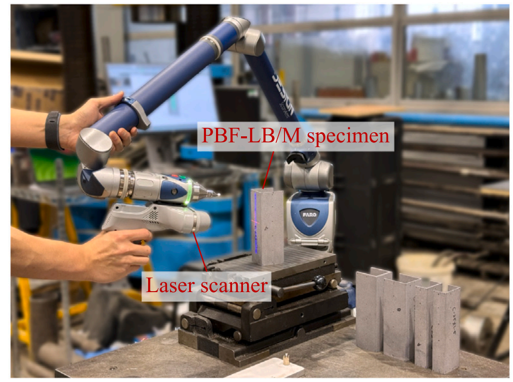

Fig. 5. 3D laser scanning of typical PBF-LB/M C-section stub column.

Table 4
Measured geometric properties of tensile coupons.

Coupon ID	W_T (mm)	t_T (mm)	A_T (mm^2)
T-3-0	9.87	2.88	28.5
T-3-45	9.89	2.98	29.5
T-3-90	9.88	2.91	28.8
T-6-0	9.87	5.77	56.9
T-6-45	9.89	5.93	58.6
T-6-90	9.89	5.90	58.3

Table 5
Measured geometric properties of the stub columns.

Specimen ID	B (mm)	H (mm)	t_f (mm)	t_w (mm)	L (mm)	$A_{density}$ (mm^2)
I-1	50.0	25.0	2.91	2.90	149.2	271.9
I-2	50.1	25.0	2.91	1.39	150.5	206.1
I-3	50.1	25.0	1.92	1.91	150.2	182.7
I-4	50.1	50.0	5.89	5.90	150.6	814.0
I-5	50.0	50.0	5.92	2.92	150.6	699.7
I-6	50.1	50.0	2.91	2.92	150.6	418.7
I-7	50.1	50.0	2.91	1.41	150.6	353.3
C-1	50.0	25.0	4.89	4.88	150.6	438.5
C-2	50.0	25.0	2.91	2.89	150.6	271.0
C-3	50.0	25.0	1.41	1.38	150.6	135.2
C-4	50.0	50.0	4.90	4.91	150.5	684.9
C-5	50.0	50.0	2.93	2.94	150.6	418.8
C-6	50.0	50.0	2.41	2.43	150.5	348.1
C-7	50.0	50.0	1.42	1.42	150.2	206.4

g/cm^3 specified in the material data sheet, implying that the adopted process parameters yielded structurally dense elements; similar values of 2.65–2.67 g/cm^3 have been reported in previous studies [17,32]. The average density-based cross-sectional area $A_{density}$ of the stub column specimens was determined by: $A_{density} = V/L$.

To accurately measure the element thickness and initial geometric imperfections of the stub columns, 3D laser scanning was performed using a FARO ScanArm with a line laser probe, featuring an accuracy of 0.1 mm and a point acquisition rate of 500,000 points per second [33] – see Fig. 5. The raw scan data, in the form of point clouds, were initially processed using Geomagic Wrap [34], in which the point clouds were converted into and exported as polygon mesh objects. These mesh models were then imported into Rhino [35] and MATLAB [36] for further post-processing. Following the methodology outlined in [37], the scanned geometries were reoriented via principal component analysis, aligning the longitudinal axis of the stub column specimens with the global x-axis. A series of contours were then created along the longitudinal direction at intervals of 0.2 mm. To isolate the plate elements (i.e. the outstand flanges and web), the tips of the flanges and the flange-to-web junctions were trimmed, retaining an effective region for each plate element for further analysis. As shown in Fig. 6, the effective region for the outstand flanges was defined as the length between points at 0.5 mm from the flange tips and 0.75 $t_{w,nom}$ from the web centreline; in the case of the webs, the effective region was specified as the length between points at 0.75 $t_{f,nom}$ from the flange centreline at both ends. The centreline geometry was obtained by averaging the trimmed contours from both sides of each plate element; then a point cloud was extracted by further gridding the trimmed contours transversely along the centrelines at a spacing of 0.2 mm. The distance between each pair of grid points was taken as the local wall thickness t_{ij}. The measured geometric properties are detailed in Table 5, where t_f and t_w are the average thicknesses of the flanges and the web, respectively, derived from the scan data.

3.2. Local geometric imperfections

The local geometric imperfections of the stub column specimens, which significantly influence the local buckling behaviour of thin-walled cross-sections [38,39], were derived based on the centreline geometry from the scan data. Three types of local geometric imperfections were considered herein – longitudinal imperfections, plate imperfections and cross-section imperfections [40]. A point cloud with a uniform spacing of 0.2 mm was extracted from the centreline geometry of each plate element. The longitudinal imperfection was defined as the deviations of the point cloud from a series of longitudinal lines fitted through the point cloud at 0.2 mm intervals [40]; the plate imperfection was defined as the deviations of the point cloud from a fitted plane, as described in [40]; the cross-section imperfection was defined as the deviations of the point cloud from the undeformed cross-section configuration along member length, with the flange-to-web junctions of the undeformed datum shape being rotated and overlapped with the boundary points of each element, as illustrated in Fig. 7. The longitudinal, plate and cross-section imperfections were denoted by ω_l, ω_p and ω_c, respectively. The local imperfection amplitudes of the outstand flanges and web are obtained and listed in Table 6, where b_f and b_w are the plate width of the flange and the web, respectively, as illustrated in Fig. 3; note that the imperfection amplitudes of the I-sections were measured over the full member length, while in the case of C-sections, the amplitudes were obtained over the length between the stiffening plates. The distributions of the longitudinal, plate and cross-section imperfections of typical column specimens (i.e. I-2, I-6, C-3 and C-6) are presented in Figs. 8 and 9, with the sign conventions illustrated in Fig. 10.

Similar patterns were observed in the longitudinal and plate imperfections of each stub column specimen, akin to the classic plate buckling shape. In the case of the cross-section imperfections, the outstand flanges of both the I- and the C-sections tend to flare outwards, deviating from the reference cross-section profile. The amplitudes of these three types of local imperfections are plotted against the width b of the corresponding plate elements in Fig. 11. To assess the level of

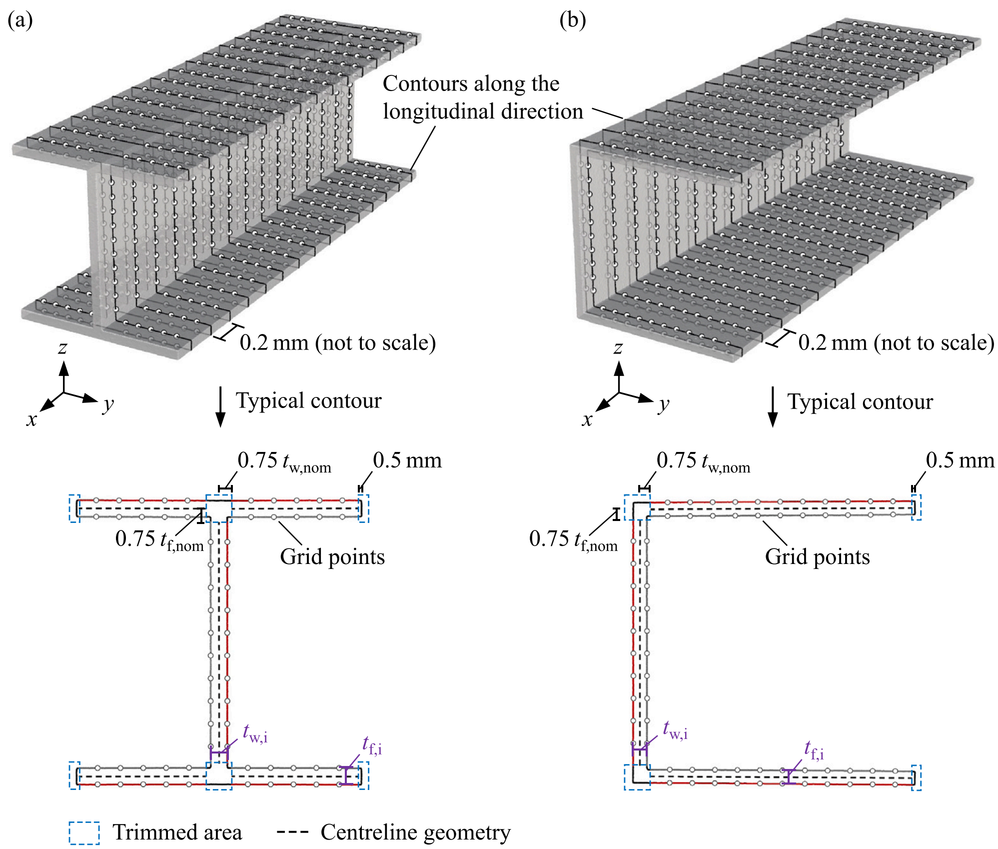

Fig. 6. Geometric analysis of typical PBF-LB/M (a) I- and (b) C-section stub column.

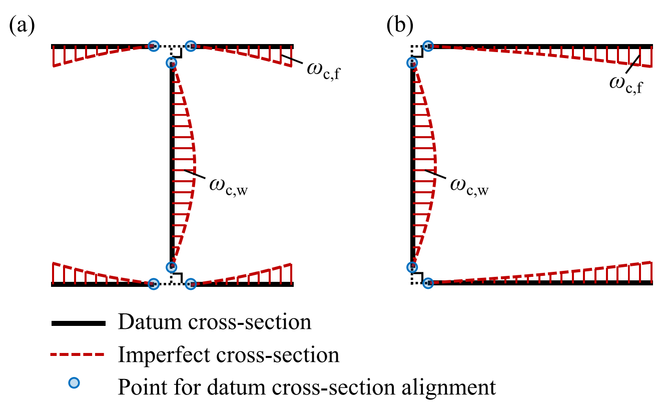

Fig. 7. Definitions of cross-section imperfection for (a) I-sections and (b) C-sections.

Table 6
Measured geometric imperfections of the PBF-LB/M I- and C-section stub columns.

Specimen ID	b_f (mm)	b_w (mm)	$\omega_{l,f}$ (mm)	$\omega_{l,w}$ (mm)	$\omega_{p,f}$ (mm)	$\omega_{p,w}$ (mm)	$\omega_{c,f}$ (mm)	$\omega_{c,w}$ (mm)
I-1	11.0	44.2	0.062	0.038	0.063	0.039	0.087	0.031
I-2	11.8	44.3	0.060	0.043	0.074	0.041	0.072	0.037
I-3	11.5	46.2	0.070	0.039	0.070	0.044	0.093	0.042
I-4	22.0	38.3	0.070	0.031	0.064	0.035	0.134	0.029
I-5	23.5	38.2	0.067	0.050	0.072	0.051	0.132	0.037
I-6	23.5	44.2	0.096	0.030	0.099	0.039	0.175	0.047
I-7	24.3	44.3	0.112	0.037	0.108	0.038	0.192	0.037
C-1	20.1	40.2	0.091	0.043	0.091	0.024	0.219	0.045
C-2	22.1	44.2	0.107	0.040	0.098	0.035	0.287	0.048
C-3	23.6	47.2	0.132	0.045	0.119	0.030	0.383	0.050
C-4	45.1	40.2	0.124	0.035	0.123	0.024	0.402	0.035
C-5	47.1	44.1	0.140	0.034	0.126	0.030	0.495	0.049
C-6	47.6	45.2	0.128	0.038	0.148	0.036	0.522	0.040
C-7	48.6	47.2	0.128	0.063	0.149	0.027	0.558	0.044

local imperfections in PBF-LB/M aluminium I- and C-sections relative to the reference values, the equivalent geometric imperfection amplitudes recommended by EN 1999-1-1:2023 (EC9) [20] for numerical simulations are utilised and presented in Fig. 11; the specified values are $b/50$ for outstand flanges and $b/200$ for internal webs. The flange elements of both the I- and C-sections generally exhibited higher local imperfection amplitudes compared to those measured in the webs, with a trend of increasing amplitude with increasing plate width. Linear regression analysis of the data revealed that the flange longitudinal and plate imperfection data points yielded similar best fit functions close to $\omega_{l,f} = \omega_{p,f} = b_f/300$, respectively, while the flange cross-section imperfection data points yield a best fit of $\omega_{c,f} = b_f/100$ which is much higher than the other two, owing to the incorporation of the out-of-squareness of the cross-sections in the imperfection measure. All the local imperfection amplitudes measured from the flanges and the webs are below the corresponding reference equivalent geometric imperfection values. The out-of-flatness of the plate in the longitudinal direction predominantly governs the local buckling behaviour of compressed stub columns, while the transverse out-of-flatness and the out-of-squareness generally have less influence on the local buckling response under longitudinal loading. Accordingly, the longitudinal imperfection amplitudes are deemed suitable for use in numerical simulations, with the elastic buckling mode being employed as the local imperfection shape. The local imperfection amplitudes of the examined PBF-LB/M I- and C-sections fall within similar ranges to those reported for conventionally extruded aluminium open sections [41–43], but are lower than those observed in DED-Arc aluminium open sections [44,45], for

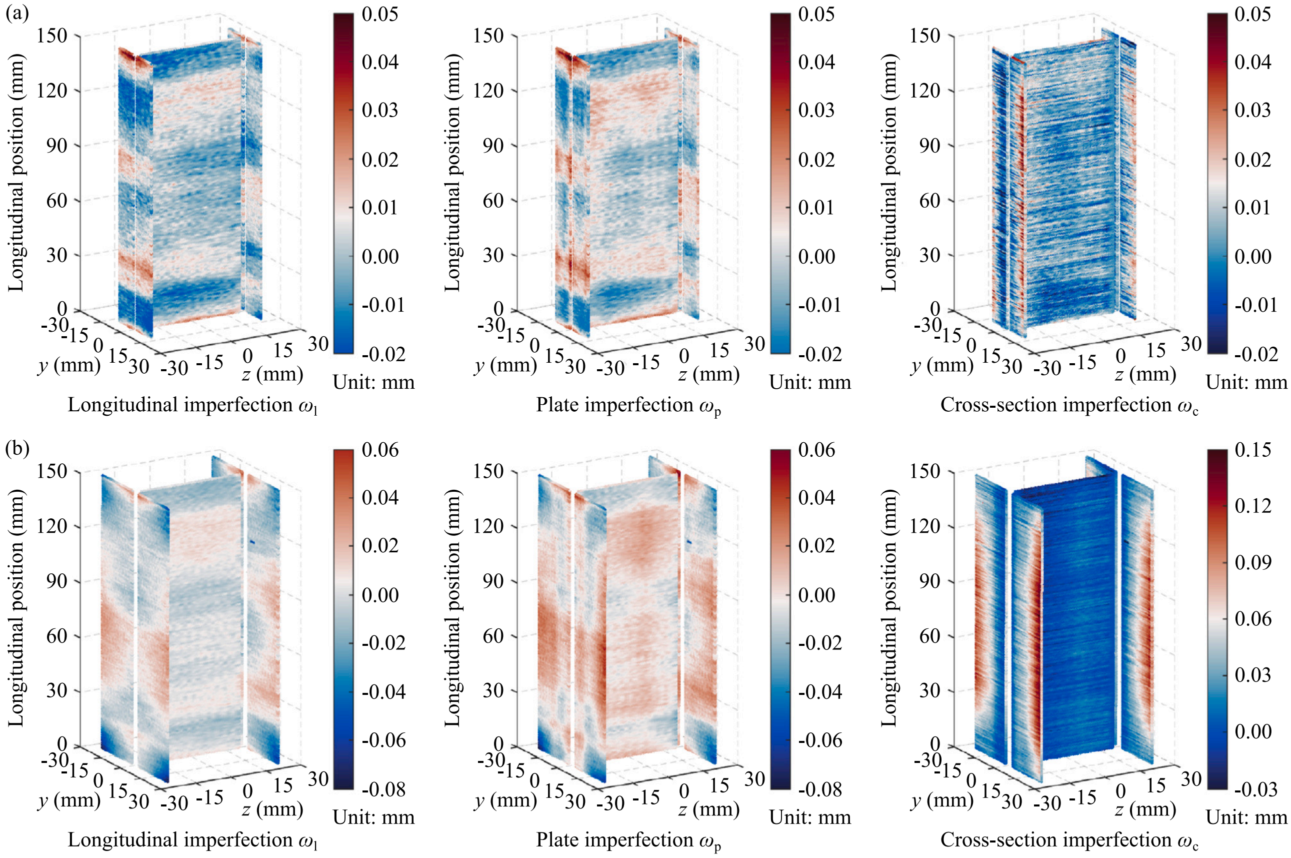

Fig. 8. Distributions of longitudinal, plate and cross-section imperfections of typical specimens: (a) I-2 and (b) I-6.

which imperfections associated with layer shifts are typically more pronounced. The measured local imperfections are reported to provide reference data for the future development of tolerances and numerical modelling. They are not explicitly incorporated in the cross-section resistance predictions of the existing design standards assessed herein (i.e. EC9, ADM, DSM and CSM).

4. Tensile coupon tests

Uniaxial tensile tests were conducted prior to the stub column tests, in compliance with EN ISO 6892-1:2019 [46], to examine the mechanical properties of the PBF-LB/M AlSi10Mg material. Six tensile coupons were tested in the Structures Laboratory of the Department of Civil and Environmental Engineering at Imperial College London; the test setup is shown in Fig. 12. The tensile coupon tests were performed using the Instron 8802 250 kN hydraulic testing machine, driven by displacement control with a strain rate of 0.007% s^{-1} being applied up to the 0.2% proof strength, and being increased to 0.025% s^{-1} from yielding to fracture, with a gradual transition through three intermediate steps [46]. A four-camera stereoscopic LaVision compact digital image correlation (DIC) system [47] was utilised, with two cameras on each side to monitor the surface deformation fields of the coupon specimens during testing. Prior to testing, a paint sprayed random white speckle pattern was applied on top of a painted matte black background within the parallel length of the coupons to provide trackable features for DIC. The applied loads were measured by a load cell built into the actuator and transmitted to the DIC system. The DIC images and the applied loads were recorded at a frequency of 2 Hz and then processed in the software DaVis 10 [48]. A similar test setup and procedure was employed in [49,50]. The engineering stress–strain responses of all coupons are plotted in Fig. 13, where the stresses were derived from the applied loads divided by the measured average cross-sectional area, and the longitudinal strains were computed and averaged over the full parallel length on both faces of each coupon specimen; the typical value of Young's modulus of conventional aluminium (i.e. E = 70 000 MPa [20]) is also presented in Fig. 13 for comparison. In general, the studied PBF-LB/M AlSi10Mg material, after heat treatment, exhibited rounded stress–strain responses, with fracture occurring without noticeable necking; the failed tensile coupons are shown in Fig. 14.

The key mechanical properties were derived from the stress–strain curves, including the Young's modulus E, the Poisson's ratio ν, the 0.2% proof strength $\sigma_{0.2}$, the 1.0% proof strength $\sigma_{1.0}$, the ultimate tensile strength σ_u, the strain at the 0.2% proof strength $\varepsilon_{0.2}$, the strain at the ultimate tensile strength ε_u, the fracture strain ε_f measured over the standard gauge length of $5.65\sqrt{A_T}$ [46] and the strain hardening exponents n and m of the two-stage Ramberg–Osgood model [51–54]. The Young's moduli E were defined as the slope of the elastic range of the stress–strain curves (i.e. the linear portion within approximately $0.1\sigma_{0.2}$–$0.3\sigma_{0.2}$); the Poisson's ratios ν were defined as the ratio of the mean transverse strain to the mean longitudinal strain within the same range. The average material properties obtained from the tensile coupon tests, grouped by the build orientation, are reported in Table 7; the test results of the individual coupon specimens are listed in Table 8.

The Young's moduli and Poisson's ratios, ranging from 73.3 GPa to 75.4 GPa and 0.32 to 0.35, respectively, are generally comparable to the results reported in previous studies on PBF-LB/M AlSi10Mg materials [17,55]; the Young's moduli are marginally higher than the typical value of 70 GPa used for conventional aluminium [20]; similar findings have been reported by Sert et al. [56] and Zhao et al. [27]. The test results for the 0.2% proof strength $\sigma_{0.2}$, varying between 205.5 MPa and 224.6 MPa, are marginally below the values reported by the manufacturer for as-built PBF-LB/M AlSi10Mg material without

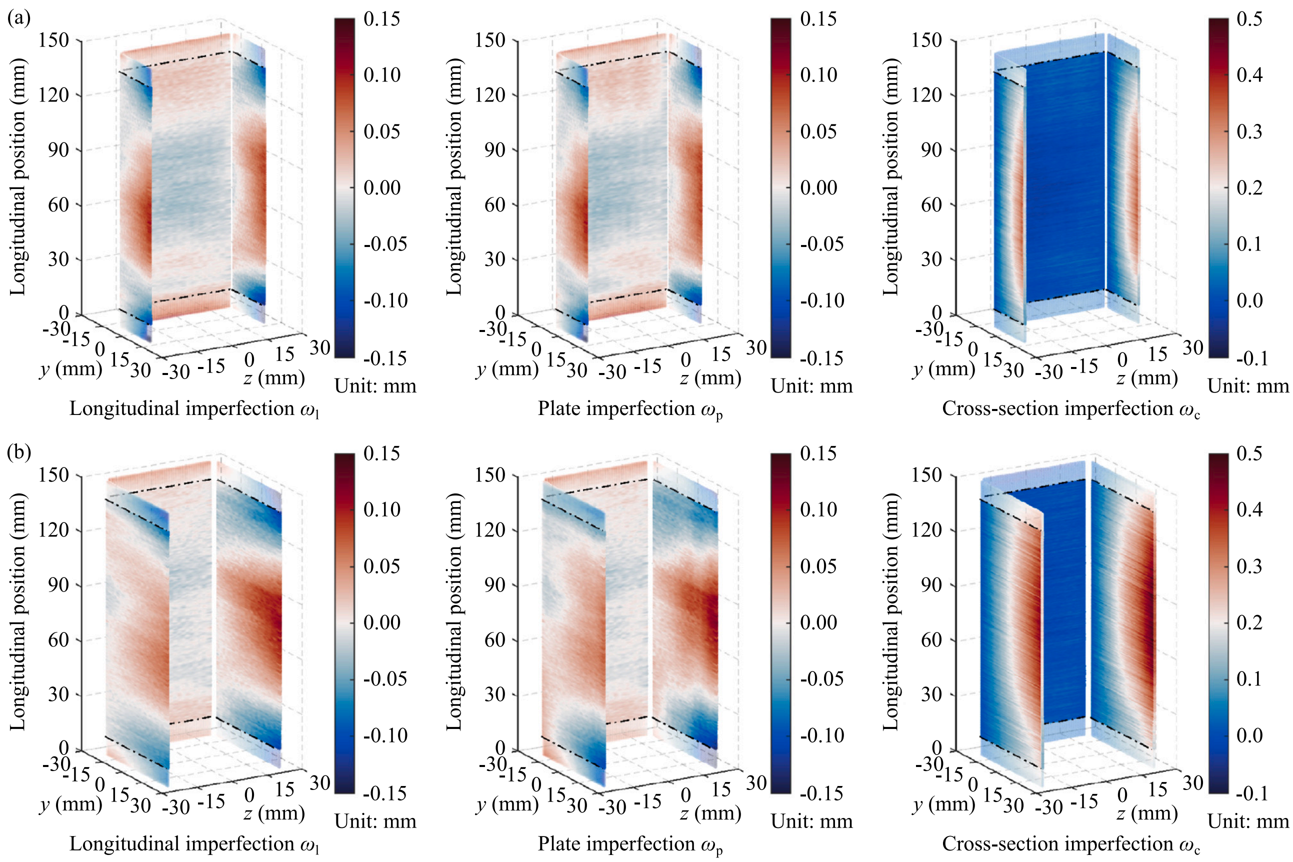

Fig. 9. Distributions of longitudinal, plate and cross-section imperfections of typical specimens: (a) C-3 and (b) C-6; member length between stiffening plates is indicated by the region between black dashed lines.

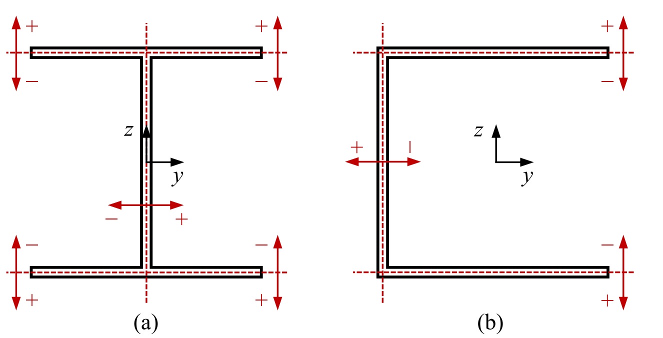

Fig. 10. Sign conventions of geometric imperfections for (a) I- and (b) C-sections.

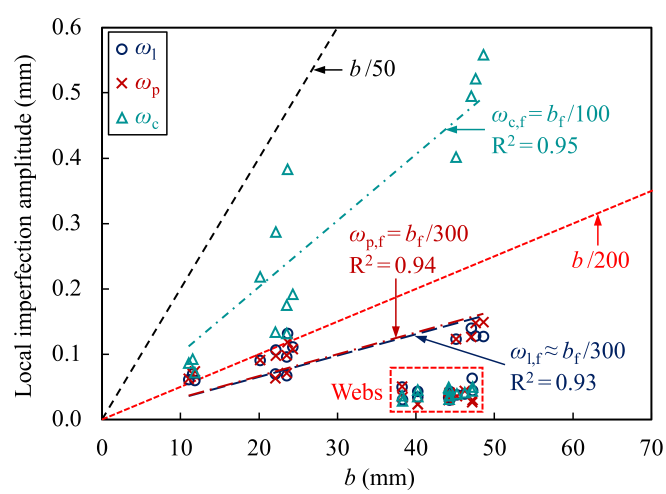

Fig. 11. Comparison of local imperfection amplitudes measured from (a) flanges and (b) webs of the examined stub column specimens, together with equivalent geometric imperfection amplitudes in EN 1999-1-1:2023 [20].

heat treatment (i.e. 270 MPa for 0° coupons and 230 MPa for 90° coupons [57]); the heat treated tensile coupons exhibited notably lower ultimate tensile strength σ_u, varying from 315.8 MPa to 329.9 MPa, than the manufacturer values for the non-heat treated material (i.e. 460 MPa for 0° coupons and 470 MPa for 90° coupons [57]), which is attributed to the coarsening of silicon particles within the alloy caused by the heat treatment [10,58]. The influence of coupon thickness on the key mechanical properties was found to be negligible, as comparable strengths and ductilities were obtained from the 3 mm and the 6 mm coupons of the same orientations. The individual mechanical properties of the tensile coupons are plotted against the coupon build orientation θ in Fig. 15. The Young's moduli and Poisson's ratios are fairly consistent across the examined build orientations. The 0° coupons exhibited superior values of the $\sigma_{0.2}$, ε_u and ε_f than the 45° and 90° coupons, while coupons with θ= 45° and 90° demonstrated similar strengths (i.e. $\sigma_{0.2}$, $\sigma_{1.0}$ and σ_u) and ductilities (i.e. ε_u and ε_f).

5. Stub column tests

5.1. Test setup

Seven I-section and seven C-section stub columns were tested to examine the local buckling behaviour of plated aluminium alloy cross-sections produced by PBF-LB/M over a wide range of local slendernesses. The stub column tests were performed using an Instron 600

Table 7
Average material properties of the tensile coupons.

θ (°)	E (MPa)	ν (–)	$\sigma_{0.2}$ (MPa)	$\sigma_{1.0}$ (MPa)	σ_u (MPa)	$\varepsilon_{0.2}$ (%)	ε_u (%)	ε_f (%)	n (–)	m (–)
0	75 400	0.32	223.5	268.0	321.9	0.50	6.3	11.7	9.1	3.9
45	74 400	0.34	211.2	262.9	320.7	0.48	5.7	7.7	6.1	3.5
90	73 300	0.35	210.7	264.9	328.2	0.49	5.3	7.3	6.1	3.4

Table 8
Key mechanical properties of the tensile coupons.

Coupon ID	E (MPa)	ν (–)	$\sigma_{0.2}$ (MPa)	$\sigma_{1.0}$ (MPa)	σ_u (MPa)	$\varepsilon_{0.2}$ (%)	ε_u (%)	ε_f (%)	n (–)	m (–)
T-3-0	75 200	0.32	224.6	268.7	322.3	0.50	6.2	12.8	10.1	4.0
T-3-45	73 400	0.33	205.5	259.5	315.8	0.48	5.5	7.3	5.8	3.5
T-3-90	73 300	0.35	208.4	263.2	326.5	0.48	5.2	7.5	6.5	3.4
T-6-0	75 600	0.33	222.4	267.4	321.4	0.49	6.5	10.7	8.0	3.8
T-6-45	75 400	0.34	216.8	266.3	325.6	0.49	5.8	8.0	6.5	3.5
T-6-90	73 300	0.34	213.0	266.6	329.9	0.49	5.5	7.0	5.8	3.4

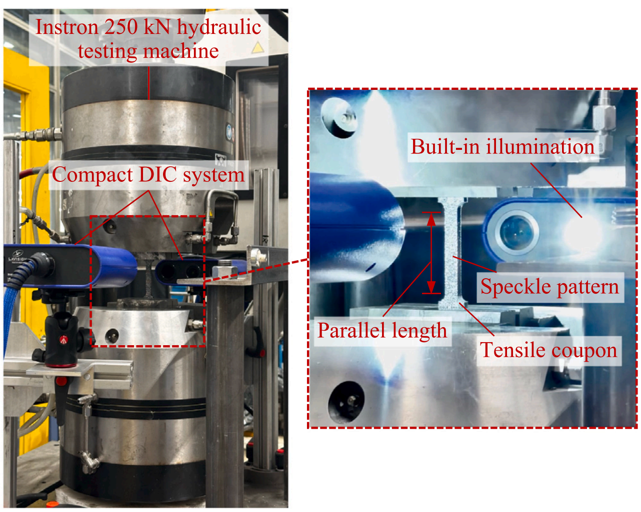

Fig. 12. Tensile coupon test setup.

kN hydraulic testing machine, driven under displacement control at a constant rate corresponding to an average compressive strain rate of 0.1% min^{-1}. The test setups for the I- and C-section stub columns are shown in Figs. 16(a) and 16(b), respectively. The stub column specimens were positioned between a pair of steel end plates to spread the load uniformly and to avoid damage to the testing machine. In the case of the I-section stub column tests, a ball seating was employed at the top of specimens, between the end plate and testing machine to accommodate any out-of-squareness at the specimen ends. Two stereoscopic LaVision compact DIC systems [47] were employed, comprising four cameras, with two cameras monitoring the flanges on the same side and the other two monitoring the web during testing. A high-contrast DIC pattern, consisting of random white speckles on a matte black background, was applied to the monitored surfaces, to facilitate the DIC feature tracking. The applied loads were measured by a load cell built into the testing machine, which were digitised and transmitted to the DIC system. The DIC images, alongside the measured loads, were acquired synchronously at a frequency of 1 Hz using the software DaVis 10 [48]. The DIC images were processed with DaVis 10 to obtain the 3D displacement fields on the monitored surfaces, with a subset size of 19 × 19 pixels containing at least three speckles within each subset, as recommended in [59,60]. Five virtual extensometers were evenly distributed along the observed length across the width of both the flanges and the web to measure the end shortening. The average axial deformation within a region that remained unbuckled at ultimate load was also determined and used to extrapolate the total end shortening, thereby accounting for the areas near both specimen ends that could not be observed by DIC [37]. The overall end shortening of each stub column was then obtained by averaging the extrapolated total end shortening values from all ten extensometers positioned on the flanges and the web.

5.2. Test results

The key test results are reported in Table 9, in which $N_{u,test}$ is the ultimate load, $\delta_{u,test}$ is the end shortening at ultimate load, β_f/ε and β_w/ε are the local slenderness of the flange and the web (Section 6.1), ρ_f and ρ_w are the local buckling factor of the flange and the web (Section 6.1), $\bar{\lambda}_L$ is the cross-sectional slenderness calculated as $\bar{\lambda}_L = \sqrt{\sigma_{0.2}/\sigma_{cr}}$, where the $\sigma_{0.2}$ is the average 0.2% proof strength obtained from the 90° coupons, and σ_{cr} is the elastic local buckling stress obtained using the finite strip software package CUFSM [61] and N_{pl} is the plastic load as given by $N_{pl} = A_{density}\sigma_{0.2}$. In the PBF-LB/M process, melt pool boundaries and interlayer regions are formed during solidification, which may contain microstructural heterogeneities or lack-of-fusion defects. When loaded parallel to the build direction, these interlayer features can act as preferential sites for strain localisation and crack initiation, leading to reduced tensile strength and ductility. The average 90° mechanical properties were adopted in the design equations, as the coupons were loaded in the same direction as the tested stub columns. Consequently, the potential weakening effects associated with the interlayer features of the PBF-LB/M process are inherently reflected in the measured material response; this approach has been successfully adopted in previous studies [18,30,62].

The failure modes of the I- and C-section stub columns at the end of the tests are shown in Fig. 19. All specimens failed by local buckling, with characteristic plate buckling half-waves developing in both the flange and web elements. The axial load–end shortening (N–δ) curves of typical stub columns (i.e. I-2, I-6, C-3 and C-6) alongside the corresponding DIC out-of-plane displacement fields at different stages (i.e. elastic stage, ultimate load and post-ultimate stage) are plotted in Figs. 17 and 18. Generally, multiple local buckling waves developed in the I-section specimens, while in the case of the C-sections, a single half-wave was typically observed in both the flanges and the web, owing to the shift of neutral axis after the flanges buckled, resulting in internal eccentricity and coupling of local buckling and global flexure, which limited the formation of additional local buckling waves. Note that specimen C-5 experienced additional end rotation due to the movement of the ball seating.

The axial load–end shortening curves of all the tested stub columns are presented in Fig. 20, with their normalised forms shown in Fig. 21, in which the axial load is normalised by the plastic load N_{pl}, and the

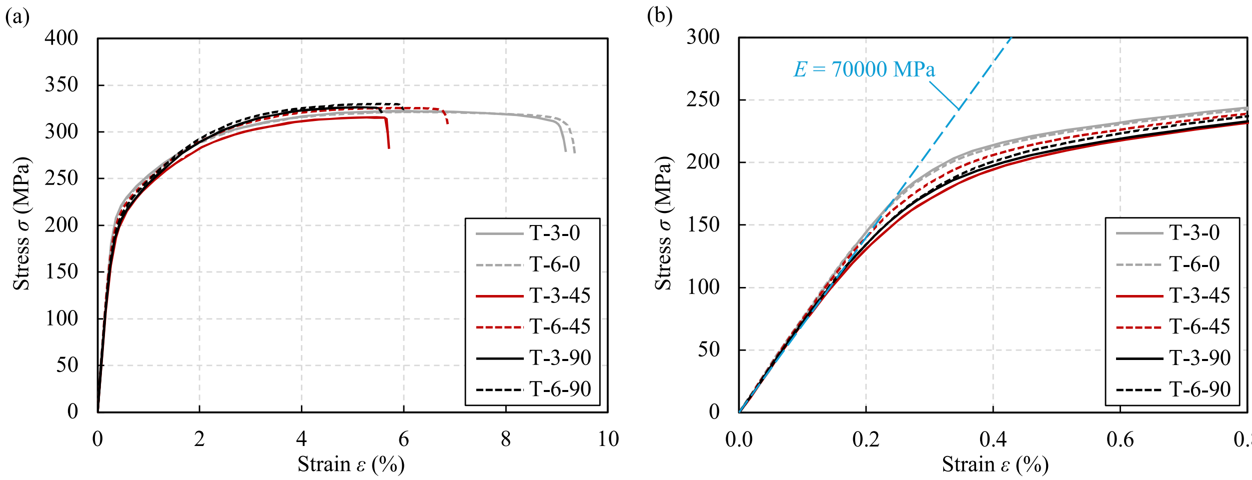

Fig. 13. Stress–strain curves of the tensile coupons over: (a) full range and (b) initial range.

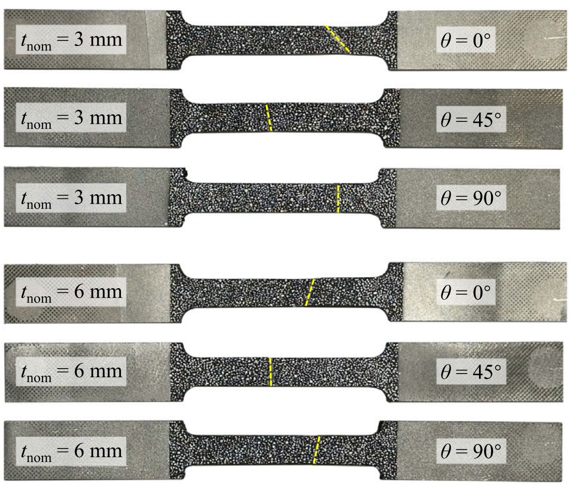

Fig. 14. Fractured tensile coupons after testing; yellow dashed lines indicate fracture locations.

end shortening is normalised by the theoretical end shortening at first yield δ_y, as determined by: $\delta_y = \sigma_{0.2}L/E$, where $\sigma_{0.2}$ and E are the average 0.2% proof strength and Young's modulus corresponding to the 90° coupons. The normalised stress–strain curves of the 90° coupons are also plotted in Fig. 21, where the stresses and strains are normalised by $\sigma_{0.2}$ and $\sigma_{0.2}/E$, respectively. At lower load levels, the initial slopes of the normalised N–δ curves closely matched the theoretical initial slope derived from the coupon tests; as the load increases, the curves start deviating from the initial slope due to the onset of local buckling or material yielding. Increasing cross-sectional slenderness led to a transition from inelastic to elastic local buckling, characterised by an earlier onset of stiffness loss in the N–δ curves and a corresponding lower normalised ultimate load. All I-section stub columns reached their plastic loads, whereas only specimens C-1, C-2 and C-4 among the C-sections attained their full plastic resistances. There was close alignment between the normalised tensile responses of the 90° coupons (i.e. T-3-90 and T-6-90) and the normalised compressive responses of the stocky specimens (i.e. I-4 and C-1), with the compressive responses exhibiting slightly more significant strain hardening after yielding [17]. Note that for each cross-section configuration, one specimen was tested owing to the high manufacturing cost associated with the PBF-LB/M process. Nevertheless, the process provides highly controlled and repeatable fabrication conditions, which generally lead to good consistency in geometric dimensions and material properties. All the stub column specimens were carefully measured and 3D scanned prior to testing, and the measured dimensions were used in the subsequent analysis to minimise uncertainty. Although the experimental scatter associated with repeated tests cannot be quantified, testing a single specimen per configuration is common practice in experimental studies on additively manufactured structural members owing to the high manufacturing cost [17,30].

6. Assessment of existing design provisions

In this section, the generated test data, together with a collated dataset from the literature, are employed to evaluate the applicability of current design provisions, i.e. EN 1999-1-1:2023, the Aluminum Design Manual 2020, the Direct Strength Method and the Continuous Strength Method, to the design of PBF-LB/M AlSi10Mg I- and C-section stub columns. The collated dataset comprises test results for conventionally-manufactured stub columns by extrusion (i.e. length-to-height ratio less than 5) from various aluminium alloy tempers and encompassing a wide range of cross-section geometries and proportions. In total, 114 I-sections [42,43,63–68] and 80 plain C-sections [65–67,69–72] are included. The examined design methods are first outlined, followed by a detailed comparison between the experimental results and the corresponding resistance predictions obtained using these design provisions.

6.1. EN 1999-1-1:2023 (EC9)

In EN 1999-1-1:2023 [20], cross-sections are categorised into four classes (i.e. Class 1–4) according to their susceptibility to local buckling, which depends on the material yield strength and the width-to-thickness ratio (b/t) of the constituent plate elements. Cross-sections of Classes 1–3 are deemed fully effective in compression, capable of attaining their full plastic resistance, while Class 4 sections are slender and typically experience local buckling prior to yielding [73]. The slenderness limits defining each cross-section class are determined according to three buckling classes (i.e. Class A, B and C), as specified in EC9, to account for the influence of material behaviour on the structural stability. The strain hardening exponent n from the Ramberg–Osgood material model is used to determine the buckling class: Class A for $n \geq 20$, Class B for $10 < n < 20$, and Class C for $n \leq 10$ [74]. Materials with lower n values exhibit an earlier onset of nonlinearity, leading to larger deformations and, consequently, higher susceptibility to local buckling. The examined PBF-LB/M AlSi10Mg material falls into Class C. According to EN 1999-1-1:2023 [20], the compressive resistance $N_{u,EC9}$ of Class 1–3 cross-sections is taken as the plastic load, whereas for Class

Table 9
Key test results of the PBF-LB/M I- and C-section stub columns.

Specimen ID	$N_{u,test}$ (kN)	$\delta_{u,test}$ (mm)	β_f/ε (–)	β_w/ε (–)	ρ_f (–)	ρ_w (–)	$\bar{\lambda}_L$ (–)	EC9 Class Flange	EC9 Class Web	$\frac{N_{u,test}}{N_{pl}}$
I-1	75.7	2.93	3.5	14.0	1.00	1.00	0.39	1	2	1.32
I-2	50.9	3.13	3.7	29.3	1.00	0.76	0.67	1	4	1.17
I-3	41.9	1.35	5.5	22.2	0.97	0.90	0.60	4	4	1.09
I-4	276.4	6.98	3.4	6.0	1.00	1.00	0.27	1	1	1.61
I-5	228.4	5.72	3.6	12.0	1.00	1.00	0.32	1	1	1.55
I-6	111.9	2.24	7.4	13.9	0.85	1.00	0.55	4	2	1.27
I-7	80.3	1.32	7.7	28.9	0.83	0.77	0.66	4	4	1.08
C-1	142.1	5.41	3.8	7.6	1.00	1.00	0.29	1	1	1.54
C-2	72.4	2.20	7.0	14.0	0.88	1.00	0.50	4	2	1.27
C-3	20.8	0.40	15.4	31.3	0.50	0.72	1.08	4	4	0.73
C-4	171.1	1.99	8.4	7.5	0.79	1.00	0.50	4	1	1.19
C-5	73.6	0.50	14.7	13.8	0.52	1.00	0.85	4	2	0.83
C-6	56.5	1.10	18.1	17.1	0.44	1.00	1.04	4	3	0.77
C-7	23.0	0.49	31.5	30.6	0.27	0.74	1.79	4	4	0.53

4 cross-sections, $N_{u,EC9}$ is determined by an effective load, as given by Eq. (1):

$$N_{u,EC9} = \begin{cases} A\sigma_{0.2} & \text{for Class 1–3 cross-sections} \\ A_{eff}\sigma_{0.2} & \text{for Class 4 cross-sections} \end{cases}, \tag{1}$$

where A is the gross cross-sectional area and $A_{eff} = \rho_c A$ is the effective cross-sectional area, with a buckling reduction factor ρ_c being applied to reduce the thickness of the constituent plate elements, thus accounting for the local buckling. The buckling reduction factor ρ_c is determined by:

$$\rho_c = \begin{cases} 1.0 & \text{for Class 1–3 elements} \\ \dfrac{C_1}{\beta/\varepsilon} - \dfrac{C_2}{(\beta/\varepsilon)^2} & \text{for Class 4 elements} \end{cases}, \tag{2}$$

where β is the width-to-thickness ratio of the plate elements, ε is the material parameter equal to $\sqrt{250/\sigma_{0.2}}$ and C_1 and C_2 are constants specified in EC9. For the examined material, falling within buckling Class C, the constants C_1 and C_2 are taken as 29 and 198 for internal elements (webs), 9 and 20 for outstand elements (flanges), respectively. In Annex H of EN 1999-1-1:2023 [20], an alternative approach is provided to assess the performance of the stocky cross-sections beyond the elastic limit. For Class 1 cross-sections, when the ultimate strain of the material is between 4% and 8%, the stress σ_5 corresponding to a strain equal to five times the yield strain $\varepsilon_y = \sigma_{0.2}/E$ is used in the design of cross-sections under axial compression. In this study, the average σ_5 value from the 90° coupons is 268.5 MPa. For the test data collated from the existing studies, where the σ_5 value is not available, $1.1\sigma_{0.2}$ is used in the resistance prediction [17]. To assess the suitability of the existing slenderness limits given in EN 1999-1-1 [20] for plated elements in pure compression, all specimens are separated into flange-critical and web-critical cases according to the elastic local buckling stresses $\sigma_{cr,p}$ of the isolated plate elements with simply supported boundary conditions, as given thus:

$$\sigma_{cr,p} = k\frac{\pi^2 E}{12\left(1-\nu^2\right)}\left(\frac{t}{b}\right)^2, \tag{3}$$

where k is taken as 0.425 for the outstand flanges (i.e. with one edge simply supported and the other free) and 4 for the internal webs (i.e. with both edges simply supported); the cross-sections with lower $\sigma_{cr,p}$ values in their flanges than in their webs are considered as flange-critical cases, while the cross-sections with lower $\sigma_{cr,p}$ in their webs than their flanges are considered as web-critical [19]. The normalised load-carrying capacities $N_{u,test}/N_{pl}$ of the flange-critical and the web-critical cases are plotted against the local slendernesses of their critical constituent plate element in Figs. 22(a) and 22(b), respectively. Generally, the normalised load-carrying capacities of the PBF-LB/M AlSi10Mg I- and C-section stub columns follow the trend of the collected conventionally-manufactured aluminium I- and C-sections. In the stocky region, the tested PBF-LB/M AlSi10Mg I- and C-section stub columns exhibit significantly higher normalised load-carrying capacities relative to the conventional counterparts owing to a more pronounced strain hardening effects associated with the examined PBF-LB/M AlSi10Mg material. In Fig. 22, the slenderness limits for both the outstand flanges and the internal webs, across the Class A, B and C materials, appear to be conservative for the collected I- and C-sections, as the majority of the test data points lie above their corresponding design curves.

The ultimate loads obtained from the generated and collated test data are normalised by the cross-section resistance calculated according to EN 1999-1-1:2023 [20] and plotted against the cross-sectional slenderness $\bar{\lambda}_L$ in Fig. 23(a), with the mean value and the coefficient of variation (COV) reported in Table 11; the detailed results of the $N_{u,test}/N_{u,EC9}$ ratio for the generated PBF-LB/M AlSi10Mg I- and C-sections are listed in Table 10, with the mean value and COV being 1.26 and 0.06, respectively. It can be seen that EN 1999-1-1 generally provided consistently safe-sided resistance predictions for both PBF-LB/M and conventionally-manufactured aluminium I- and C-sections. The conservatism is attributed partly to the conservative slenderness limits for both outstand and internal elements of I- and C-sections, which could be potentially modified to achieve more accurate resistance predictions.

6.2. Aluminum design manual 2020 (ADM)

According to the American Aluminum Design Manual 2020 [21], the local buckling resistance is obtained by applying strength reduction to the slender elements, unlike EC9, in which the thicknesses of the slender elements are reduced. A Weighted Average Method is adopted to calculate the local buckling strength $N_{u,ADM}$ of compressed cross-sections, as expressed by Eq. (4):

$$N_{u,ADM} = \sum_{i=1}^{n}\sigma_{c,i}A_i + \sigma_{0.2}\left(A - \sum_{i=1}^{n}A_i\right), \tag{4}$$

where A_i is the area of element i and $\sigma_{c,i}$ is the local buckling stress of element i, which is determined based on the element slenderness ratio, as given by Eq. (5):

$$\sigma_{c,i} = \begin{cases} \sigma_{0.2} & \text{for } \dfrac{b}{t} \le \lambda_1 \\ B_p - \eta D_p\dfrac{b}{t} & \text{for } \lambda_1 < \dfrac{b}{t} < \lambda_2 \\ \dfrac{k_2\sqrt{B_p E}}{\eta b/t} & \text{for } \dfrac{b}{t} \ge \lambda_2 \end{cases}, \tag{5}$$

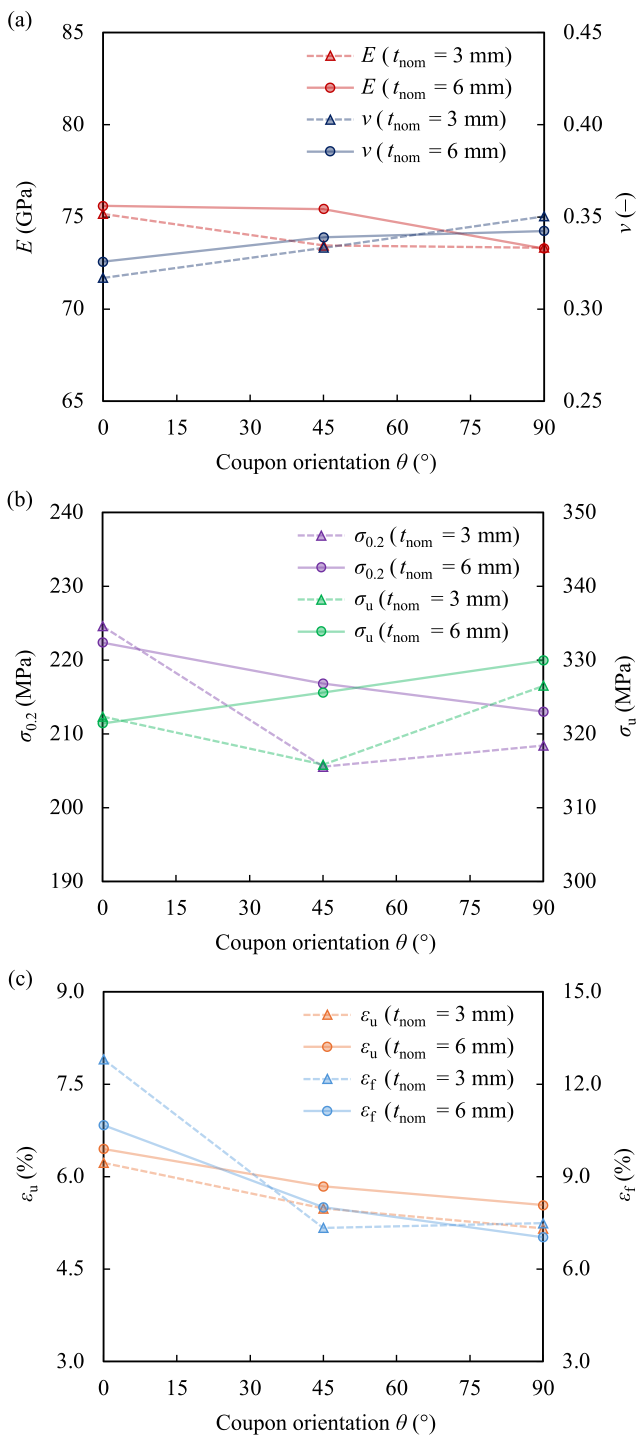

Fig. 15. Variation of key mechanical properties with coupon orientation θ.

where $\lambda_1 = \left(B_p - \sigma_{0.2}\right)/\eta D_p$ and $\lambda_2 = k_1 B_p/\eta D_p$ are the slenderness limits corresponding to the yielding and the inelastic buckling limit states, respectively; k_1 and k_2 are the post-buckling constants, taken as 0.50 and 2.04, respectively; the coefficient η is taken as 5.0 for flanges (outstand elements) and 1.6 for webs (internal elements); B_p and D_p are the buckling constants, as determined by:

$$B_p = \sigma_{0.2}\left(1 + \left(\frac{\sigma_{0.2}}{440\kappa}\right)^{1/3}\right), \quad (6)$$

$$D_p = \frac{B_p}{20}\left(\frac{6B_p}{E}\right)^{1/2}, \quad (7)$$

Table 10
Comparisons of the test results with resistance predictions from EC9, ADM, DSM and CSM for the PBF-LB/M I- and C-section stub columns.

Specimen ID	$N_{u,test}/N_{u,EC9}$	$N_{u,test}/N_{u,ADM}$	$N_{u,test}/N_{u,DSM}$	$N_{u,test}/N_{u,CSM}$
I-1	1.32	1.32	1.32	0.93
I-2	1.26	1.22	1.19	1.17
I-3	1.15	1.09	1.08	1.05
I-4	1.26	1.61	1.61	1.03
I-5	1.21	1.54	1.54	0.99
I-6	1.41	1.30	1.27	1.18
I-7	1.31	1.15	1.10	1.07
C-1	1.20	1.53	1.53	0.99
C-2	1.33	1.26	1.26	1.12
C-3	1.17	1.07	1.01	1.00
C-4	1.37	1.26	1.18	1.04
C-5	1.20	1.15	0.95	0.95
C-6	1.21	1.18	1.02	1.02
C-7	1.22	1.15	1.19	1.11
Mean	1.26	1.27	1.23	1.05
COV	0.06	0.14	0.17	0.07

where κ is equal to 6.895.

The ultimate loads obtained from the test dataset normalised by the ADM design predictions are plotted against $\bar{\lambda}_L$ in Fig. 23; the values of the $N_{u,test}/N_{u,ADM}$ ratios of the generated and collated test data are reported in Tables 10 and 11, where the mean ratio $N_{u,test}/N_{u,ADM}$ of the tested PBF-LB/M AlSi10Mg stub columns is 1.27, with a COV of 0.14. In comparison with EC9, the ADM does not account for the significant strain hardening effects of the examined PBF-LB/M AlSi10Mg material, leading to more conservative resistance predictions for the very stocky columns. However, the yield slenderness limits λ_1 for outstand and internal elements are less conservative than those of EC9, as indicated in Fig. 22, resulting in more accurate predictions for both the PBF-LB/M and conventionally-manufactured aluminium I- and C-sections.

6.3. Direct strength method (DSM)

The Direct Strength Method [21] predicts the compressive resistance of cross-sections directly as a function of their full cross-section elastic buckling stress, instead of reducing thickness or buckling stress at plate element level, thus element interaction effects are taken into account. The DSM has been incorporated in the Aluminum Design Manual 2020 [21], and is used as an alternative simplified approach for cross-section design. The buckling resistance predicted by the DSM $N_{u,DSM}$ is given by:

$$N_{u,DSM} = \sigma_c A, \quad (8)$$

where σ_c is the local buckling stress of the cross-section, as defined in Eq. (9):

$$\sigma_c = \begin{cases} \sigma_{0.2} & \text{for } \lambda_{eq} \le \lambda_3 \\ B_p - D_p\lambda_{eq} & \text{for } \lambda_3 < \lambda_{eq} < \lambda_4 \\ \dfrac{k_2\sqrt{B_p E}}{\lambda_{eq}} & \text{for } \lambda_{eq} \ge \lambda_4 \end{cases}. \quad (9)$$

in which $\lambda_3 = B_p - \sigma_{0.2}D_p$ and $\lambda_4 = k_1 B_p D_p$ are the slenderness limits for yielding and inelastic buckling, B_p and D_p are the buckling constants, as given by Eqs. (6) and (7), $\lambda_{eq} = \pi\sqrt{E/\sigma_{cr}}$ is the equivalent slenderness, and σ_{cr} is the elastic local buckling stress obtained using the finite strip software package CUFSM [61]. Fixed-Fixed boundary conditions were assumed in the elastic buckling analysis, with the allowance of multiple buckling waves to be developed along the member length. The elastic local buckling stress σ_{cr} was taken as the elastic

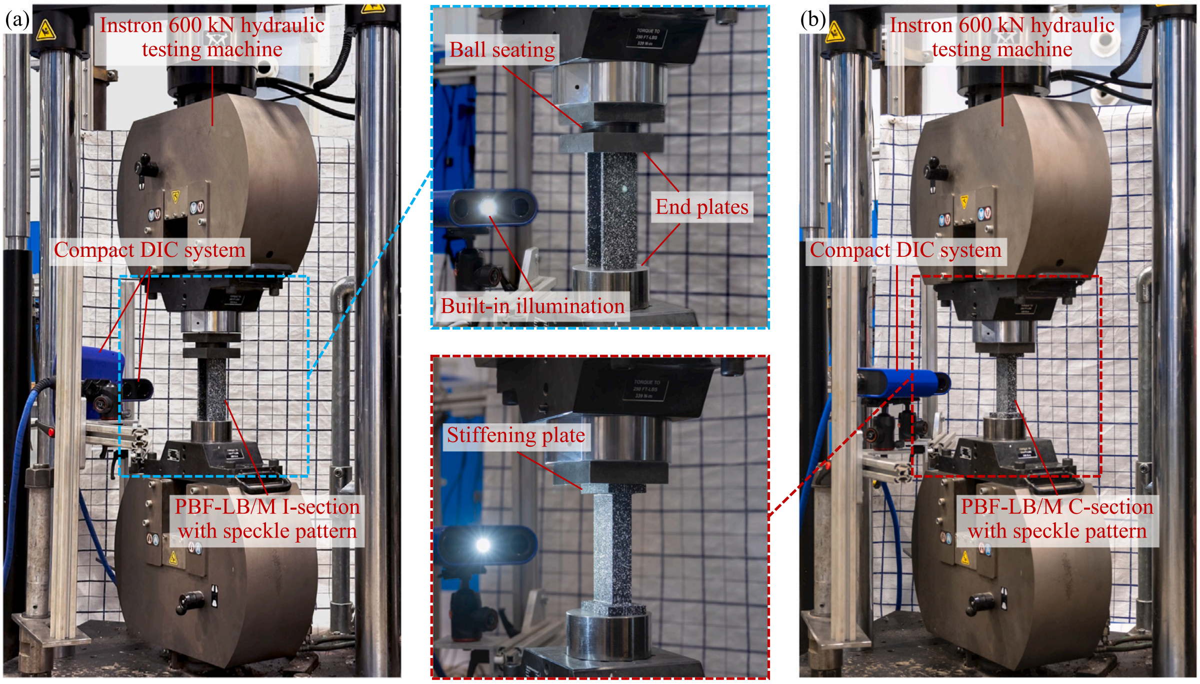

Fig. 16. Stub column test setup for (a) I-sections and (b) C-sections.

Table 11
Comparisons of the test results with resistance predictions according to EC9, ADM, DSM and CSM for PBF-LB/M and conventional aluminium stub columns.

Manufacturing method	No. of data	Evaluation parameter	$\frac{N_{u,test}}{N_{u,EC9}}$	$\frac{N_{u,test}}{N_{u,ADM}}$	$\frac{N_{u,test}}{N_{u,DSM}}$	$\frac{N_{u,test}}{N_{u,CSM}}$
PBF-LB/M aluminium	14	Mean COV	1.26 0.06	1.27 0.14	1.23 0.17	1.05 0.07
Conventional aluminium	180	Mean COV	1.16 0.07	1.13 0.08	1.12 0.07	1.11 0.07
All test data	194	Mean COV	1.16 0.07	1.14 0.09	1.13 0.09	1.10 0.07

buckling stress of the most critical local buckling mode. The load-carrying capacities of all the test data are normalised by the resistance predictions determined according to the DSM $N_{u,DSM}$, and are plotted against the local slenderness in Fig. 23, with the mean value and COV of $N_{u,test}/N_{u,DSM}$ reported in Table 11. With the incorporation of the element interaction effects, the DSM resistance predictions are generally less conservative than the design predictions according to EC9 and ADM, except in the stocky range, where the strain hardening effects are not taken into account.

6.4. Continuous strength method (CSM)

The Continuous Strength Method [22,75,76] is a deformation-based design approach that replaces conventional cross-section classification with a continuous base curve defining the limiting strain ε_{csm} that a cross-section can sustain before failure, expressed as a function of cross-sectional slenderness $\bar{\lambda}_L$. By incorporating an elastic–linear hardening material model, the CSM accounts for strain hardening, enabling more accurate and rational predictions of cross-section resistance. The method is particularly effective for nonlinear materials such as aluminium and stainless steel [77–79], and can be directly applied within the framework of design by advance analysis [80–82]. The CSM base curve for plated cross-sections is defined through the ratio of the limiting strain ε_{csm} to the yield strain ε_y, as given by Eq. (10):

$$\frac{\varepsilon_{csm}}{\varepsilon_y} = \begin{cases} \frac{0.25}{\bar{\lambda}_L^{3.6}} \le \min\left(15, \frac{C_3\varepsilon_u}{\varepsilon_y}\right) & \text{for } \bar{\lambda}_L \le 0.68 \\ \left(1 - \frac{0.222}{\bar{\lambda}_L^{1.05}}\right)\frac{1}{\bar{\lambda}_L^{1.05}} & \text{for } 0.68 < \bar{\lambda}_L \le 1.60 \end{cases}, \quad (10)$$

where C_3 is a coefficient corresponding to the adopted CSM material model, taken as 0.5 for aluminium alloys [83–85]. The CSM cross-section compression resistance is given by:

$$N_{u,csm} = \begin{cases} A\sigma_{csm} & \text{for } \bar{\lambda}_L \le 0.68 \\ \frac{\varepsilon_{csm}}{\varepsilon_y} A\sigma_{0.2} & \text{for } 0.68 < \bar{\lambda}_L \le 1.60 \end{cases}, \quad (11)$$

where σ_{csm} is the CSM limiting stress, as given by Eq. (12):

$$\sigma_{csm} = \begin{cases} E\varepsilon_{csm} & \text{for } \varepsilon_{csm} < \varepsilon_y \\ \sigma_{0.2} + E_{sh}\left(\varepsilon_{csm} - \varepsilon_y\right) & \text{for } \varepsilon_y \le \varepsilon_{csm} \le C_4\varepsilon_u \end{cases}, \quad (12)$$

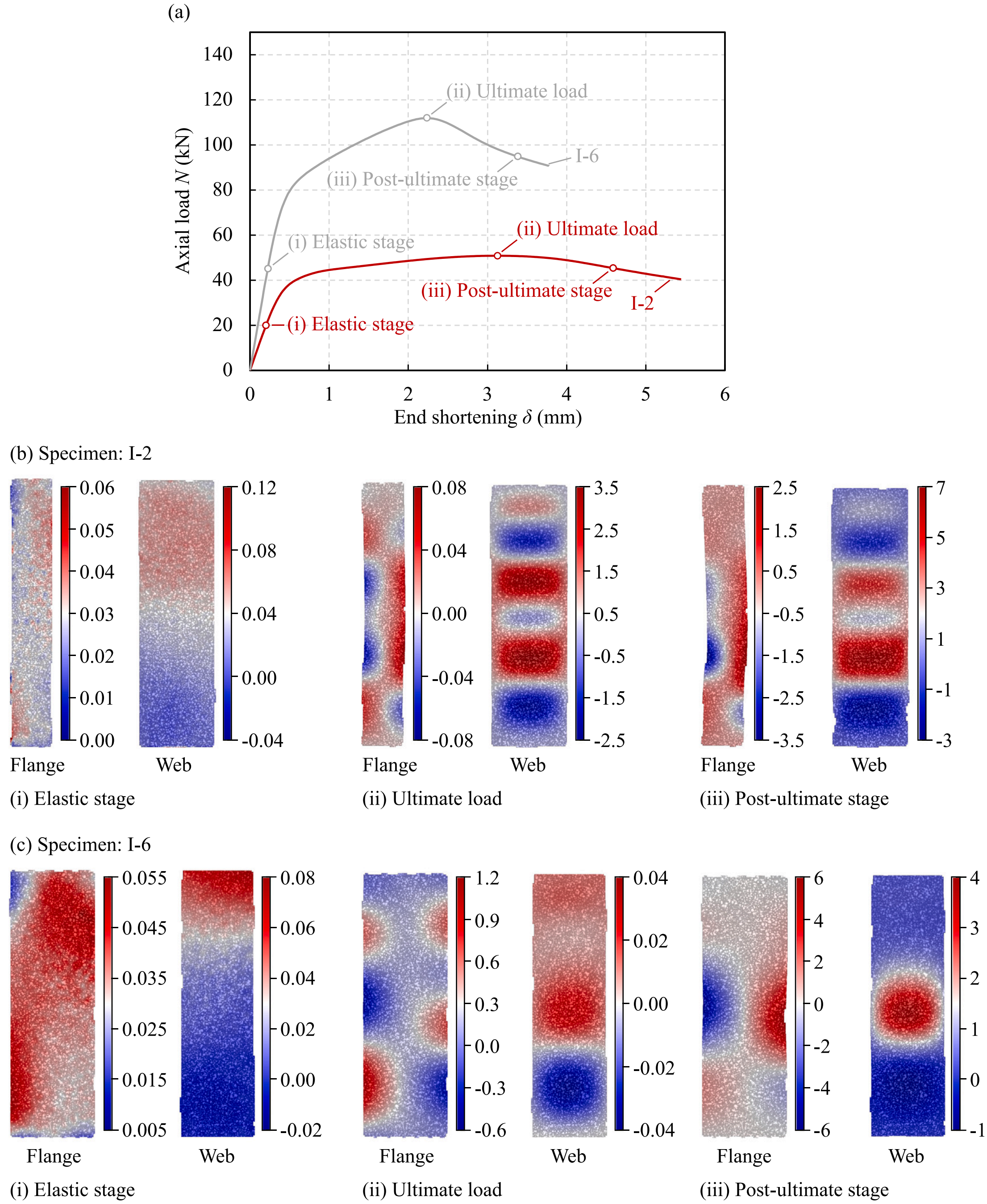

Fig. 17. (a) Load–end shortening curves and out-of-plane displacement fields obtained from DIC for typical buckling modes of specimen (b) I-2 and (c) I-6 at different load levels (unit: mm).

with the coefficient $C_4 = 0.5$ and the strain hardening slope $E_{sh} = (\sigma_u - \sigma_{0.2}) / (C_4\varepsilon_u - \varepsilon_y)$ [85].

Fig. 24 shows the measured values of $\varepsilon_{csm}/\varepsilon_y$ from the test specimens versus their corresponding cross-sectional slenderness $\bar{\lambda}_L$, alongside the base curve derived from Eq. (10). The base curve developed for conventionally manufactured aluminium sections [86] provides safe-sided estimates of the deformation capacity for PBF-LB/M aluminium cross-sections. The data point that deviates from the base curve corresponds to specimen I-2, which exhibited a relatively large end shortening at the ultimate load. The relatively narrow flanges of I-2 provide less restraint to its web edges, resulting in a less stiff post-buckling response and allowing multiple buckling waves to develop in the web, as shown in Fig. 17(b). In this case, the post-buckling deformation is distributed along the web rather than concentrated in a single dominant buckle, leading to a slightly larger end shortening at the ultimate load than other specimens of similar cross-sectional slenderness. Despite the deviation of this data point from the base curve, the resistance is nonetheless accurately predicted by the CSM. The experimental load-carrying capacities of the generated and collated test data are normalised by the plastic loads, and are plotted against cross-sectional slenderness $\bar{\lambda}_L$ in Fig. 25, alongside the CSM design curve derived using the measured material properties of the examined PBF-LB/M AlSi10Mg material. It can be seen that most of the test data points of the tested PBF-LB/M AlSi10Mg stub columns lie above the design curve, indicating that the CSM generally provides safe-sided

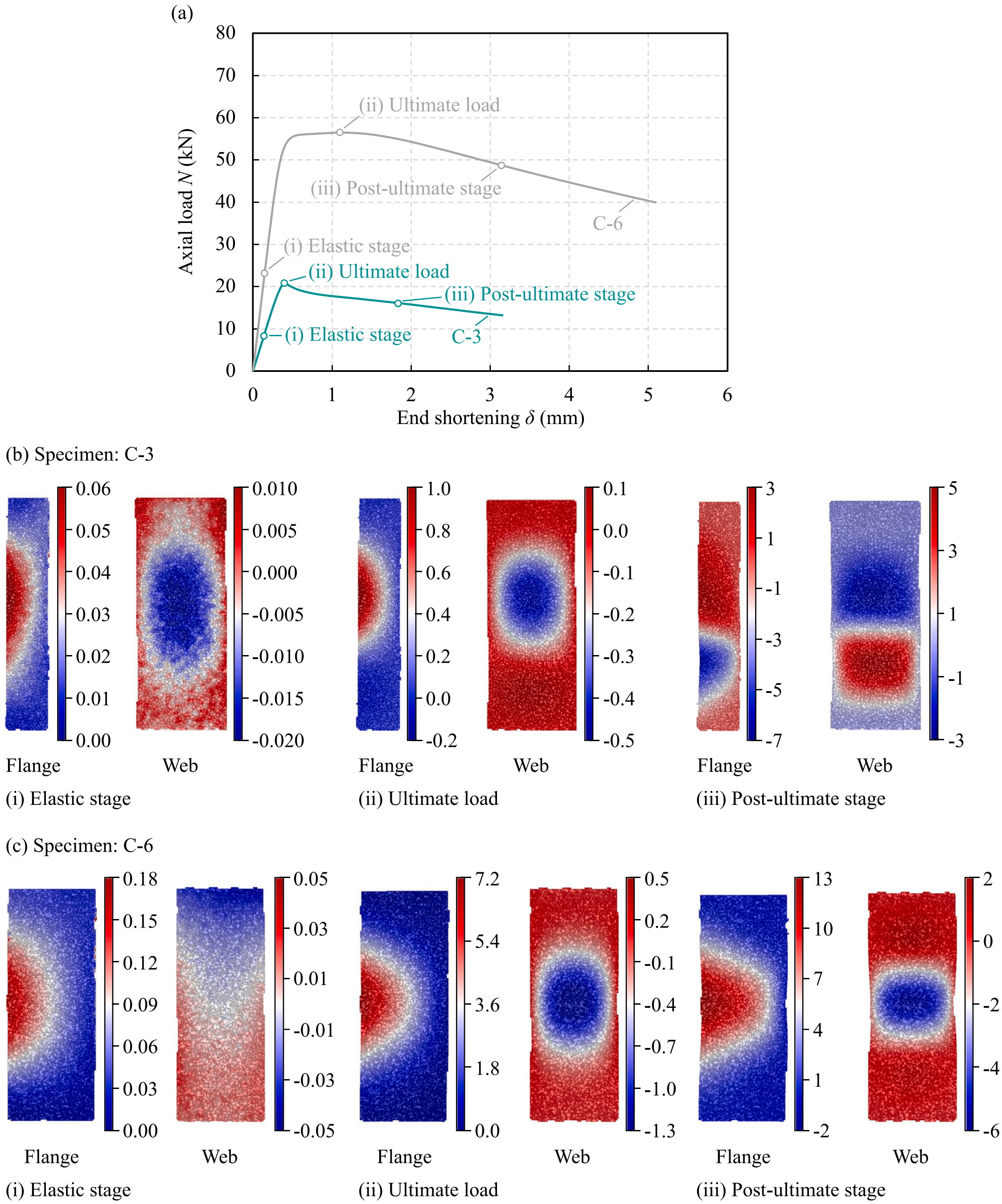

Fig. 18. (a) Load–end shortening curves and out-of-plane displacement fields obtained from DIC for typical buckling modes of specimen (b) C-3 and (c) C-6 at different load levels (unit: mm).

resistance predictions for the examined PBF-LB/M AlSi10Mg I- and C-sections. The ratios of the load-carrying capacity to the CSM resistance predictions of the generated and collated test data are reported in Tables 10 and 11. The mean value and COV of $N_{u,test}/N_{u,CSM}$ are 1.05 and 0.07 of the PBF-LB/M AlSi10Mg I- and C-sections examined in this study; in the case of the collected conventional aluminium I- and C-sections, the mean value and COV of $N_{u,test}/N_{u,CSM}$ are 1.11 and 0.07, respectively. For both the conventionally-manufactured and the PBF-LB/M aluminium, the CSM yields more accurate and less scattered resistance predictions, compared with EC9, ADM and DSM, particularly in the case of the studied PBF-LB/M aluminium which exhibited pronounced strain hardening.

7. Conclusions

An experimental investigation into the local buckling behaviour of aluminium I- and C-section stub columns manufactured by laser beam powder bed fusion (PBF-LB/M) using AlSi10Mg powder has been presented. A total of seven I-sections and seven C-sections, covering a wide range of plate width-to-thickness ratios, were fabricated, heat treated and tested under axial compression. Tensile coupons were produced and tested at 0°, 45° and 90° orientations relative to the scanning direction, from which the key mechanical properties were obtained. The results demonstrated that the PBF-LB/M AlSi10Mg material had an almost isotropic elastic response after heat treatment. Prior to testing, 3D laser scanning was utilised to measure the geometric dimensions and initial geometric imperfections of the stub

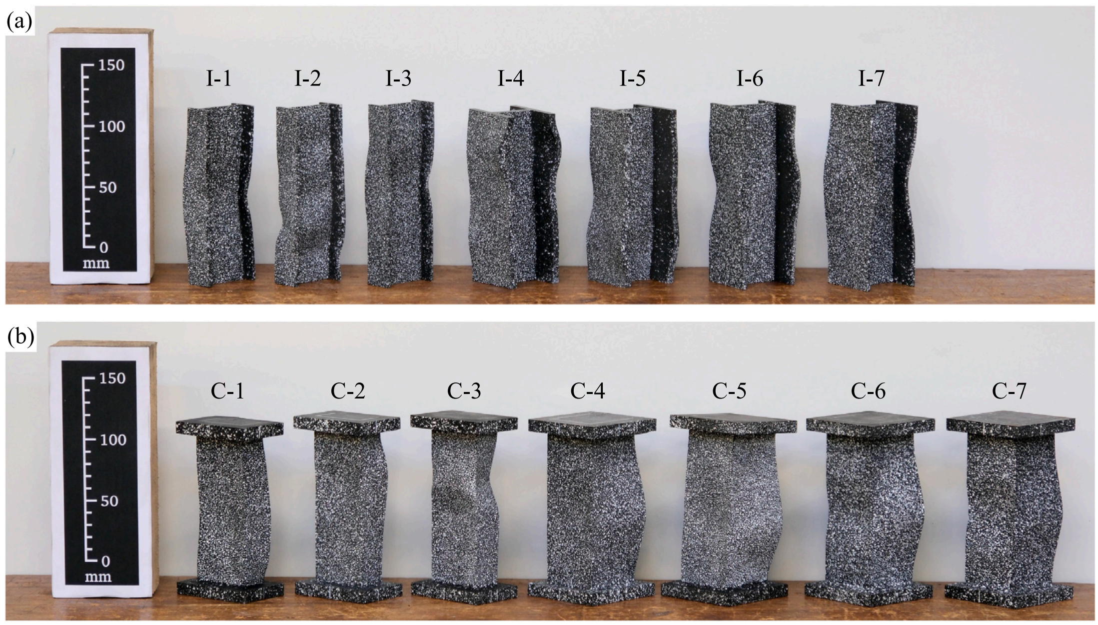

Fig. 19. Failure modes of (a) I- and (b) C-section stub columns.

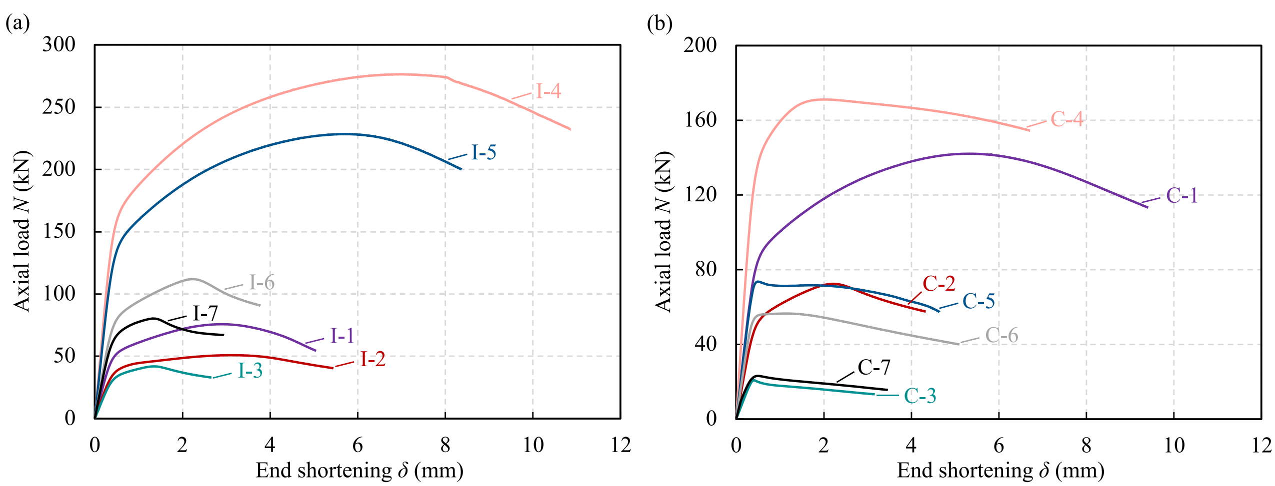

Fig. 20. Load–end shortening curves: (a) I- and (b) C-section stub columns.

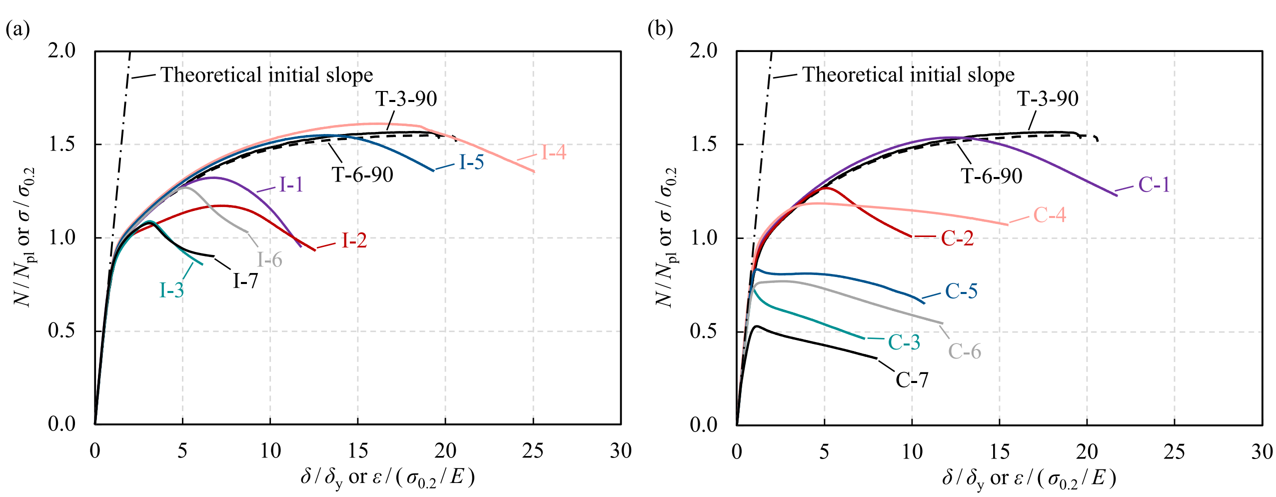

Fig. 21. Normalised load–end shortening curves: (a) I- and (b) C-section stub columns.

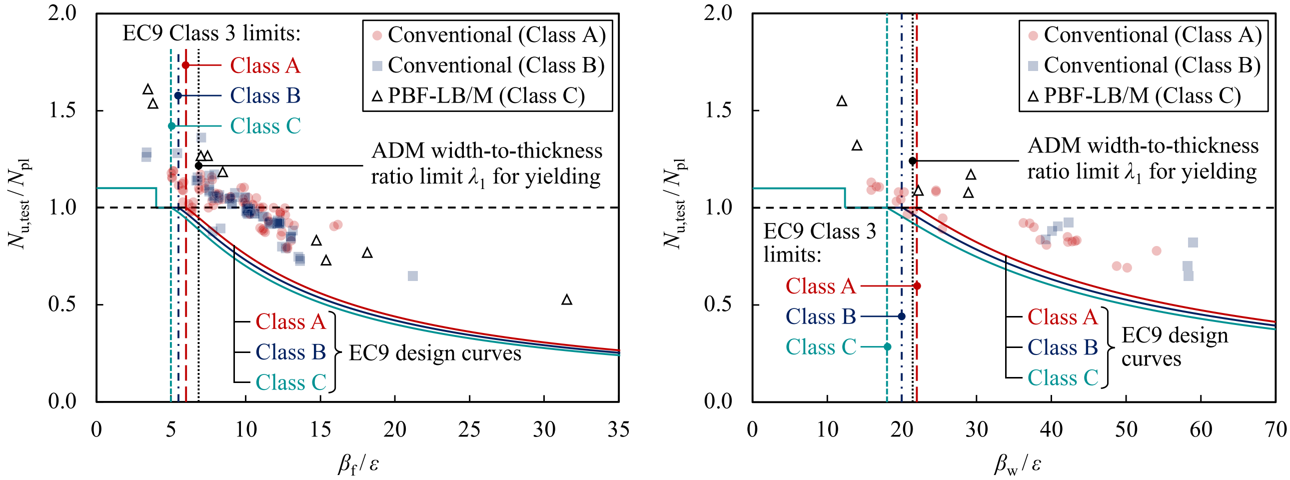

(a) Flange-critical cases (b) Web-critical cases

Fig. 22. Normalised load-carrying capacity versus local slenderness and EC9 design curves for (a) flange-critical cases and (b) web-critical cases.

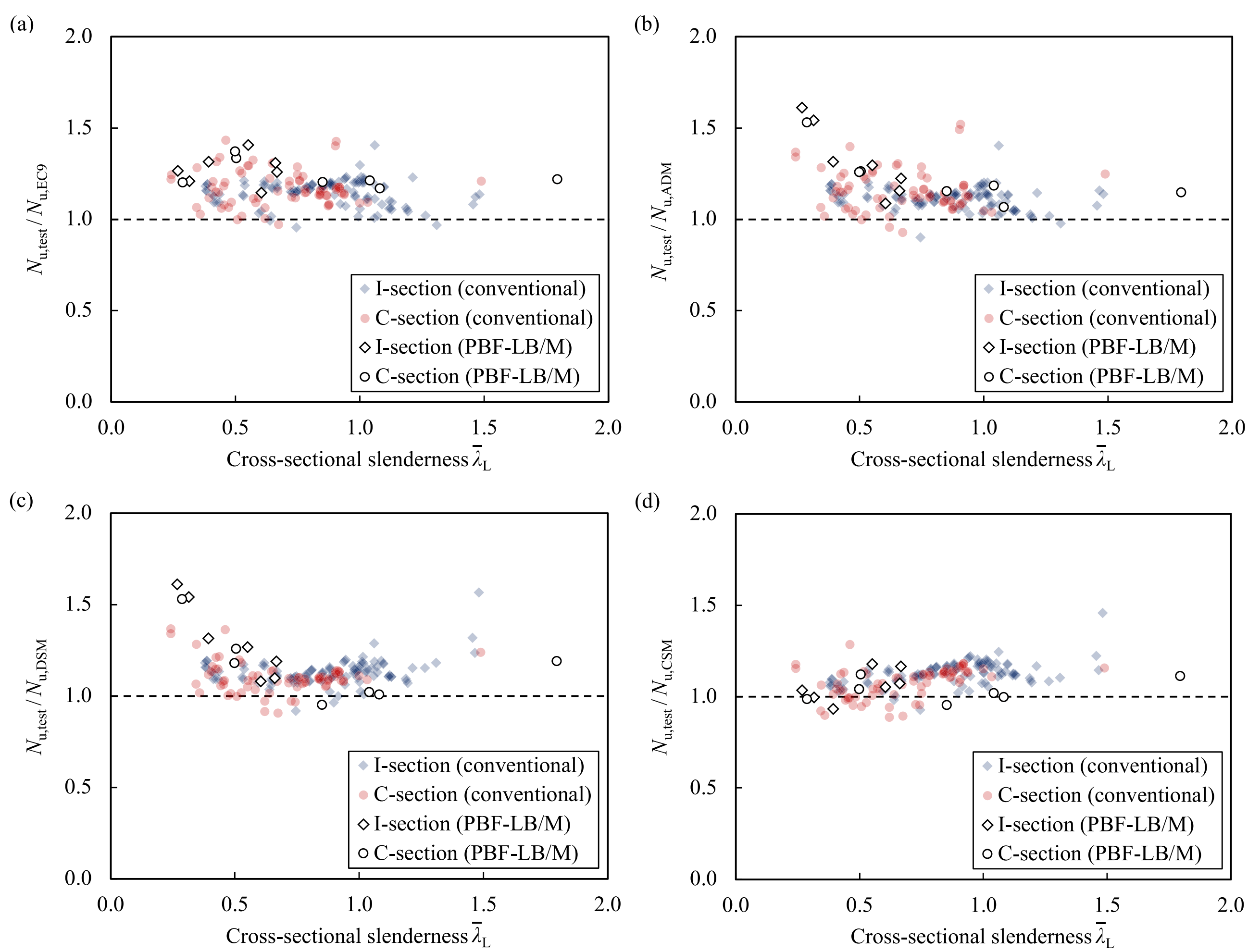

Fig. 23. Comparisons of the test results with the design predictions according to: (a) EN 1999-1-1:2023, (b) Aluminum Design Manual 2020, (c) the Direct Strength Method and (d) the Continuous Strength Method.

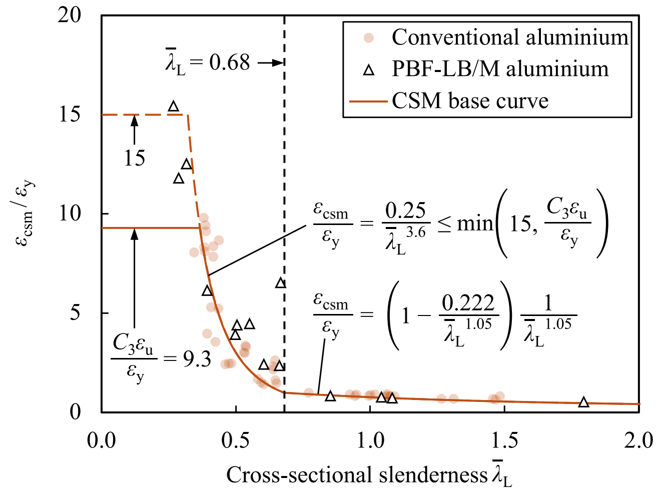

Fig. 24. Comparison of the experimental deformation capacities with the CSM base curve.

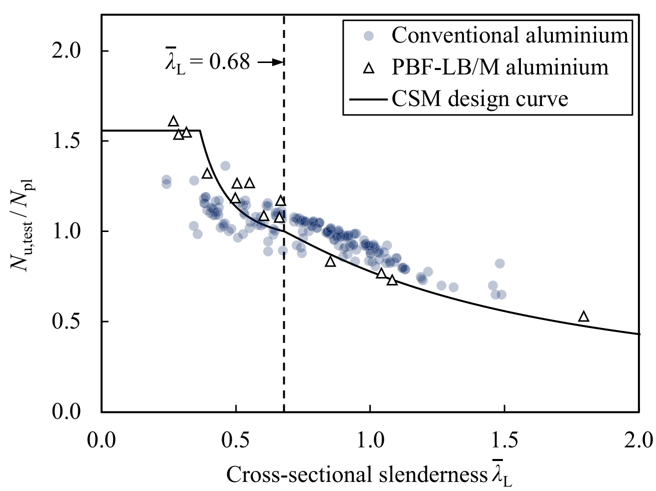

Fig. 25. Comparisons of the test results with the CSM design curve.

column test specimens. The initial geometric imperfections of the examined PBF-LB/M I- and C-sections were found to resemble the elastic local buckling modes of the plate elements, while the measured amplitudes are generally below the values recommended for numerical modelling in EN 1999-1-1:2023. The local imperfection amplitudes of the PBF-LB/M aluminium I- and C-sections are comparable to those measured from conventionally extruded aluminium open sections, but lower than those reported for DED-Arc aluminium open sections. Stub column tests were then performed to investigate the local buckling responses and load-carrying capacities of the PBF-LB/M aluminium sections, with their surface deformation monitored using digital image correlation (DIC). All tested specimens failed by local buckling, and the experimental results showed the expected reduction in normalised load-carrying capacity with increasing local slenderness, reflecting the increasing dominance of local buckling. For the more stocky (compact) cross-sections, pronounced strain hardening was observed, leading to enhanced ultimate loads. The load-carrying capacities of the PBF-LB/M aluminium stub columns, along with collated existing test data for conventionally-manufactured aluminium I- and C-sections, were compared against the design resistance predictions obtained using EN 1999-1-1:2023 (EC9), the Aluminum Design Manual 2020 (ADM), the Direct Strength Method (DSM) and the Continuous Strength Method (CSM). Overall, all four design approaches provided generally safe-sided predictions, among which the CSM yielded the most accurate and consistent resistance estimates for both the additively manufactured and conventionally-manufactured aluminium sections, owing to its continuous nature and the explicit consideration of strain hardening effects. The experimental results provide valuable benchmark data for PBF-LB/M aluminium structural cross-sections and enhance understanding of their local buckling behaviour and structural performance. The findings support the applicability of existing aluminium design methods to additively manufactured sections, while demonstrating the superior accuracy of advanced approaches (i.e. CSM) in capturing the beneficial strain hardening effects.

CRediT authorship contribution statement

Wenxuan Hong: Writing – original draft, Visualization, Software, Methodology, Investigation, Formal analysis, Data curation. **Eman Mansour:** Writing – review & editing, Visualization, Investigation, Data curation, Conceptualization. **Marina Bock:** Writing – review & editing, Supervision, Resources, Project administration, Methodology, Funding acquisition, Data curation, Conceptualization. **Leroy Gardner:** Writing – review & editing, Visualization, Supervision, Resources, Project administration, Methodology, Investigation, Conceptualization.

Declaration of competing interest

The authors declare that they have no known competing financial interests or personal relationships that could have appeared to influence the work reported in this paper.

Acknowledgements

The research presented in this paper has received pump prime funds from the University of Wolverhampton, United Kingdom under the Lord Paul Swarj scheme. The lead author gratefully acknowledges the Skempton Scholarship from Imperial College London, United Kingdom and the funding from the China Scholarship Council (CSC) for financial support. The second author gratefully acknowledges financial support from the Department of Academic Attachés and Scholarship Affairs, funded by the Ministry of Higher Education, Government of Libya. The authors thank Mr. Neil Bassini and Dr. John Robinson for their support during the additive manufacturing of the samples.

Data availability

Data will be made available on request.

References

[1] Gardner L. Metal additive manufacturing in structural engineering–review, advances, opportunities and outlook. Structures 2023;47:2178–93.
[2] Kyvelou P, Spinasa A, Gardner L. Testing and analysis of optimized wire arc additively manufactured steel trusses. J Struct Eng 2024;150(3):04024008.
[3] Gardner L, Li J, Meng X, Huang C, Kyvelou P. I-section steel columns strengthened by wire arc additive manufacturing-concept and experiments. Eng Struct 2024;306:117763.
[4] EN ISO/ASTM 52900 2021. Additive manufacturing - general principles - fundamentals and vocabulary. In: Standard. Brussels: European Committee for Standardisation; 2021.
[5] Zuo W, Chen MT, Zhao O, Gardner L. Parametric optimization-based design and testing of 3D printed stainless steel circular X-joints. Eng Struct 2026;353:122148.
[6] Heinz A, Haszler A, Keidel C, Moldenhauer S, Benedictus R, Miller WS. Recent development in aluminium alloys for aerospace applications. Mater Sci Eng: A 2000;280(1):102–7.
[7] Rambabu P, P. N Eswara, Kutumbarao VV, Wanhill RJH. Aluminium alloys for aerospace applications. Aerosp Mater Mater Technol: Vol 1: Aerosp Mater 2016;29–52.
[8] Wang Z, Li M, Han Q, Yun X, Zhou K, Gardner L, Mazzolani FM. Structural fire behaviour of aluminium alloy structures: Review and outlook. Eng Struct 2022a;268:114746.

[9] Read N, Wang W, Essa K, Attallah MM. Selective laser melting of AlSi10Mg alloy: Process optimisation and mechanical properties development. Mater Des (1980-2015) 2015;65:417–24.
[10] Rosenthal I, Shneck R, Stern A. Heat treatment effect on the mechanical properties and fracture mechanism in alsi10mg fabricated by additive manufacturing selective laser melting process. Mater Sci Eng: A 2018;729:310–22.
[11] Serjouei A, Libura T, Brodecki A, Radziejewska J, Broniszewska P, Pawłowski P, Szymczak T, Bodaghi M, Kowalewski ZL. Strength-hardness relationship for AlSi10Mg alloy produced by laser powder bed fusion: An experimental study. Mater Sci Eng: A 2022;861:144345.
[12] Gadlegaonkar N, Bansod PJ, Lakshmikanthan A, Bhole K. A review on additively manufactured AlSi10Mg alloy: Mechanical, tribological, and microstructure properties. J Mines, Met Fuels 2025;73(1).
[13] Costas M, Morin D, de Lucio M, Langseth M. Testing and simulation of additively manufactured AlSi10Mg components under quasi-static loading. Eur J Mech A Solids 2020;81:103966.
[14] Gite RE, Wakchaure VD. A review on process parameters, microstructure and mechanical properties of additively manufactured AlSi10Mg alloy. Mater Today: Proc 2023;72:966–86.
[15] San BB, Cheng X, Shan ZW, Qiu Y. Study on optimization method of axially compressed SLM manufacturing free corrugated square tubes. J Constr Steel Res 2026;238:110213.
[16] Bock M, Bawazeer J, Robinson J, Theofanous M, Skalomenos K. Structural performance of additive manufactured aluminum tubular stub columns. Ce/Papers 2023;6(3–4):751–6.
[17] Zhang R, Amraei M, Piili H, Gardner L. Testing of additively manufactured aluminium material and cross-sections in compression. Eng Struct 2025;341:120798.
[18] Mansour E, Ruan X, Rossi B, Robinson J, Arjunan A, Bock M. Behaviour of 3D printed Al7075 square hollow sections in compression. Ce/Papers 2025;8(6):37–42.
[19] Gardner L, Fieber A, Macorini L. Formulae for calculating elastic local buckling stresses of full structural cross-sections. Structures 2019a;17:2–20.
[20] EN 1999-1-1 2023. Eurocode 9 - design of aluminium structures - part 1-1: general structural rules. In: Standard. Brussels: European Committee for Standardisation; 2023.
[21] Aluminum Design Manual 2020. Aluminum design manual – part 1 specification for aluminum structures. In: Standard. Arlington: The Aluminum Association; 2020.
[22] Gardner L. The continuous strength method. In: Proceedings of the Institution of Civil Engineers-Structures and Buildings, vol. 161, (3):2008, p. 127–33.
[23] EOS GmbH. EOS M 290. 2025, URL https://www.eos.info/metal-solutions/metal-printers/eos-m-290. [Accessed 12th August 2025].
[24] Chen B, Moon SK, Yao X, Bi G, Shen J, Umeda J, Kondoh K. Strength and strain hardening of a selective laser melted AlSi10Mg alloy. Scr Mater 2017;141:45–9.
[25] J.G.S. Macías T Douillard, Zhao L, Maire E, Pyka G, Simar A. Influence on microstructure, strength and ductility of build platform temperature during laser powder bed fusion of AlSi10Mg. Acta Mater 2020;201:231–43.
[26] Wu H, Ren Y, Ren J, Liang L, Li R, Fang Q, Cai A, Shan Q, Tian Y, Baker I. Selective laser melted AlSi10Mg alloy under melting mode transition: Microstructure evolution, nanomechanical behaviors and tensile properties. J Alloys Compd 2021;873:159823.
[27] Zhao L, Song L, J.G.S. Macías Y Zhu, Huang M, Simar A, Li Z. Review on the correlation between microstructure and mechanical performance for laser powder bed fusion AlSi10Mg. Addit Manuf 2022;56:102914.
[28] Ziemian RD. Guide to stability design criteria for metal structures. New York: John Wiley & Sons; 2010.
[29] Huntsman. Araldite 2011. 2025, URL https://www.huntsman.com/products/araldite2000/araldite-2011. [Accessed on 31 July 2025].
[30] Hong W, Zhang R, Hadjipantelis N, Gardner L. Buckling behaviour and design of DED-arc high strength steel circular hollow sections. Thin-Walled Struct 2025a;114297.
[31] Hong W, Kyvelou P, Zhang R, Gardner L. Mechanical testing and microstructural analysis of wire laser beam directed energy deposited steel plates. Mater Des 2025b;255:114141.
[32] Mathe NR, Tshabalala LC. The validation of the microstructural evolution of selective laser-melted AlSi10Mg on the in-house built machine: energy density studies. Prog Addit Manuf 2019;4(4):431–42.
[33] FARO. ScanArms. 2024, URL https://www.faro.com. [Accessed on 31st July 2025].
[34] Oqton Inc. Geomagic wrap 2017. 2017, URL https://www.oqton.com/geomagic-wrap. [Accessed on 31 July 2025].
[35] Robert McNeel & Associates. Rhino 6. 2018, URL https://www.rhino3d.com/. [Accessed on 31st July 2025].
[36] The Mathworks Inc. MATLAB:R2024a. 2024, URL https://uk.mathworks.com. [Accessed on 31 July 2025].
[37] Weber B, Meng X, Gardner L. Local buckling behaviour of wire arc additively manufactured steel I-sections under axial compression and combined loading. Thin-Walled Struct 2025;211:113027.
[38] Yuan H, Wang Y, Gardner L, Shi Y. Local–overall interactive buckling of welded stainless steel box section compression members. Eng Struct 2014;67:62–76.
[39] Zhao O, Rossi B, Gardner L, Young B. Behaviour of structural stainless steel cross-sections under combined loading–part II: Numerical modelling and design approach. Eng Struct 2015;89:247–59.
[40] Meng X, Gardner L. Testing of hot-finished high strength steel SHS and RHS under combined compression and bending. Thin-Walled Struct 2020;148:106262.
[41] Wang Z, Zhan L, Yun X. Experimental study of local buckling behaviour of 7A04-T6 high strength aluminium alloy H-section stub columns in fire. Eng Struct 2024;317:118631.
[42] Yuan H, Wang Y, Chang T, Du X, Bu Y, Shi Y. Local buckling and postbuckling strength of extruded aluminium alloy stub columns with slender I-sections. Thin-Walled Struct 2015;90:140–9.
[43] Zhi X, Wang Y, Zhang Y, Li B, Ouyang Y. Study of local buckling performance of 7075-T6 high-strength aluminium alloy H-section stub columns. Thin-Walled Struct 2022;180:109925.
[44] Li J, Jiang K, Wang Z, Chen MT, Zhao O. Geometric properties and cross-section behaviour of wire arc additively manufactured AA5356 I-section and cruciform-section stub columns. Eng Struct 2026a;351:121977.
[45] Li J, Wang Z, Chen MT, Su A, Zhao O. Wire arc additively manufactured aluminium alloy open sections: 3D geometric analysis and compressive behaviour. Thin-Walled Struct 2026b;114687.
[46] EN ISO 6892-1:2019. Metallic materials - tensile testing - part 1: method of test at room temperature. In: Standard. Brussels: European Committee for Standardisation; 2019.
[47] LaVision GmbH. 2D-/3D stereo digital image correlation. 2025, URL https://www.lavision.de/en/. [Accessed on 31 July 2025].
[48] LaVision GmbH. DaVis 10. 2021, URL https://www.lavision.de/en/products/davis-software. [Accessed on 31st July 2025].
[49] Guo X, Kyvelou P, Ye J, Teh LH, Gardner L. Experimental investigation of wire arc additively manufactured steel single-lap shear bolted connections. Thin-Walled Struct 2022;181:110029.
[50] Guo X, Kyvelou P, Ye J, Teh LH, Gardner L. Experimental study of DED-arc additively manufactured steel double-lap shear bolted connections. Eng Struct 2023;281:115736.
[51] Ramberg W, Osgood WR. Description of stress–strain curves by three parameters. Technical report, Washington, D. C., USA: National Advisory Committee for Aeronautics; 1943.
[52] Mirambell E, Real E. On the calculation of deflections in structural stainless steel beams: an experimental and numerical investigation. J Constr Steel Res 2000;54(1):109–33.
[53] Yun X, Wang Z, Gardner L. Full-range stress–strain curves for aluminum alloys. J Struct Eng 2021;147(6):04021060.
[54] Kucukler M, Xing Z, Gardner L. Behaviour and design of stainless steel I-section columns in fire. J Constr Steel Res 2020;165:105890.
[55] Hitzler L, Janousch C, Schanz J, Merkel M, Heine B, Mack F, Hall W, Öchsner A. Direction and location dependency of selective laser melted AlSi10Mg specimens. J Mater Process Technol 2017;243:48–61.
[56] Sert E, Hitzler L, Hafenstein S, Merkel M, Werner E, Öchsner A. Tensile and compressive behaviour of additively manufactured AlSi10Mg samples. Prog Addit Manuf 2020;5(3):305–13.
[57] EOS GmbH. Material data sheet – flexline – EOS aluminium AlSi10Mg. Technical report, München, Germany: EOS GmbH – Electro Optical Systems; 2024.
[58] Wang CG, Zhu JX, Wang GW, Qin Y, Sun MY, Yang JL, Shen XF, Huang SK. Effect of building orientation and heat treatment on the anisotropic tensile properties of AlSi10Mg fabricated by selective laser melting. J Alloys Compd 2022b;895:162665.
[59] Jones EMC, Iadicola MA, editors. In: A good practices guide for digital image correlation, vol. 10, New York: Springer; 2018.
[60] Meng X, Pullen A, Guo X, Yun X, Gardner L. 3D laser scanning and DIC in structural testing: state-of-the-art, best practice and effective use. Eng Struct 2025;345:121055.
[61] Li Z, Schafer BM. Buckling analysis of cold-formed steel members with general boundary conditions using CUFSM: conventional and constrained finite strip methods. In: Proceedings of the 20th international specification conference on cold-formed steel structures. St. Louis: Missouri University of Science and Technology; 2010, p. 17–31.
[62] Bawazeer J, Theofanous M, Cabrera M, Skalomenos K, Bock M. Compression response of additive manufactured AlSi10Mg square and rectangular hollow sections. Ce/Papers 2025;8(6):73–8.
[63] Yan J, Kong G, Wang Z, Zhang L, Wang X. Compression behaviours of aluminium alloy I-column at low temperatures. Structures 2022;44:418–35.
[64] Dahboul S, Li L, Verma P, Dey P, Boissonnade N. Experimental investigations on the local stability of aluminium I-Sections. 2025, Available at SSRN 5173686.
[65] Heimerl GJ, Roy JA. Column and plate compressive strengths of aircraft structural materials: Extruded 75S-T aluminum alloy. Natl Advis Comm Aeronaut 1945.
[66] Heimerl GJ, Fay D. Column and plate compressive strengths of aircraft structural materials: Extruded R303-T aluminum alloy. Natl Advis Comm Aeronaut 1945.
[67] Heimerl GJ, Niles DE. Column and plate compressive strengths of aircraft structural materials: Extruded 14S-T aluminum alloy. Natl Advis Comm Aeronaut 1946.

[68] Pisapia A, Fabbrocino F, Piluso V. Testing and analysis of aluminium H-sections subjected to local buckling. J Constr Steel Res 2026;236:110025.

[69] Mennink J. Cross-sectional stability of aluminium extrusions: prediction of the actual local buckling behaviour (Ph.D. thesis), Department ArGEnCo, Technische Universiteit Eindhoven; 2002.

[70] Zhu J, Li Z, Su MN, Young B. Behaviour of aluminium alloy plain and lipped channel columns. Thin-Walled Struct 2019;135:306–16.

[71] Georgantzia E, Gkantou M, Kamaris GS. Aluminium alloy channel columns: Testing, numerical modelling and design. Thin-Walled Struct 2023;182:110242.

[72] Sun Y, Fu Z, Song Y, Xia J. Cross-sectional behavior of aluminum alloy channel section stub columns after exposure to fire. J Struct Eng 2023;149(7):04023085.

[73] Gardner L, Chan TM. Cross-section classification of elliptical hollow sections. Steel Compos Struct 2007;7(3):185.

[74] Misiek T, Norlin B, Höglund T. European buckling curves for aluminium compression members: A review of proposals for revision. Ce/Papers 2019;3(3–4):563–70.

[75] Liew A, Gardner L. Ultimate capacity of structural steel cross-sections under compression, bending and combined loading. Structures 2015;1:2–11.

[76] Zhao O, Gardner L, Young B. Behaviour and design of stainless steel SHS and RHS beam–columns. Thin-Walled Struct 2016a;106:330–45.

[77] Ashraf M, Gardner L, Nethercot DA. Structural stainless steel design: Resistance based on deformation capacity. J Struct Eng 2008;134(3):402–11.

[78] Bock M, Gardner L, Real E. Material and local buckling response of ferritic stainless steel sections. Thin-Walled Struct 2015;89:131–41.

[79] Zhao O, Rossi B, Gardner L, Young B. Experimental and numerical studies of ferritic stainless steel tubular cross sections under combined compression and bending. J Struct Eng 2016;142(2):04015110.

[80] Gardner L, Yun X, Fieber A, Macorini L. Steel design by advanced analysis: material modeling and strain limits. Engineering 2019;5(2):243–9.

[81] Fieber A, Gardner L, Macorini L. Design of structural steel members by advanced inelastic analysis with strain limits. Eng Struct 2019;199:109624.

[82] Walport F, Gardner L, Nethercot DA. Equivalent bow imperfections for use in design by second order inelastic analysis. Structures 2020;26:670–85.

[83] Su MN, Young B, Gardner L. Testing and design of aluminum alloy cross sections in compression. J Struct Eng 2014;140(9):04014047.

[84] Su MN, Young B, Gardner L. Flexural response of aluminium alloy SHS and RHS with internal stiffeners. Eng Struct 2016a;121:170–80.

[85] Gardner L, Yun X, Walport F. The continuous strength method–review and outlook. Eng Struct 2023;275:114924.

[86] Su MN, Young B, Gardner L. The continuous strength method for the design of aluminium alloy structural elements. Eng Struct 2016b;122:338–48.